Petrological constraints on the tectonic setting of the Kathmandu Nappe in the Langtang-Gosainkund-Helambu regions, Central Nepal Himalaya

PETROLOGICAL CONSTRAINTS ON THE TECTONIC SETTING OF THE KATHMANDU NAPPE IN THE LANGTANG–GOSAINKUND–HELAMBU REGIONS, CENTRAL NEPAL HIMALAYA

G. Rapa[1], C. Groppo[1,2], P. Mosca[2], F.Rolfo[1,2]

1 – Department of Earth Sciences, University of Torino, Via Valperga Caluso 35, 10125 Turin, Italy
2 – IGG-CNR, Via Valperga Caluso 35, 10125 Turin, Italy

Corresponding author mail id:- chiara.groppo@unito.it

ABSTRACT

The Gosainkund–Helambu region in central Nepal occupies a key area for the development of Himalayan kinematic models, connecting the well-investigated Langtang area to the north with the Kathmandu Nappe, whose interpretation is still debated, to the south. In order to understand the structural and metamorphic architecture of the Greater Himalayan Sequence (GHS) in this region, a detailed petrological study was performed, focusing on selected metapelite samples from both the Gosainkund–Helambu and Langtang transects. The structurally lowest sample investigated belongs to the Lesser Himalayan Sequence (LHS); its metamorphic evolution is characterized by a narrow hairpin *P*–*T* path with peak *P*–*T* conditions of 595 ± 25 °C, 7.5 ± 1 kbar. All of the other samples here investigated belong to the GHS. Along the Langtang section, two tectono-metamorphic units have been distinguished within the GHS: the Lower Greater Himalayan Sequence (L–GHS), characterized by peak *P*–*T* conditions at 728 ± 11 °C, 10 ± 0.5 kbar (corresponding to a *T*/depth ratio of 22 ± 1 °C km^{-1}), and the structurally higher Upper Greater Himalayan Sequence (U–GHS), with peak metamorphic conditions at 780 ± 20 °C, 7.8 ± 0.8 kbar (corresponding to a *T*/depth ratio of 31 ± 4 °C km^{-1}). This confirms the existence of a main tectono-metamorphic discontinuity within the GHS, as previously suggested by other authors. The results of petrological modelling of the metapelites from the Gosainkund–Helambu section show that this region is entirely comprised within a sub-horizontal and thin L–GHS unit: the estimated peak metamorphic conditions of 734 ± 19 °C, 10 ± 0.8 kbar correspond to a uniform *T*/depth ratio of 23 ± 3 °C km^{-1}. The metamorphic discontinuity identified along the Langtang transect and dividing the GHS in two tectono-metamorphic units is located at a structural level too high to be intersected along the Gosainkund–Helambu section. Our results have significant implications for the interpretation of the Kathmandu Nappe (KN) and provide a contribution to the more general discussion of the Himalayan kinematic models. We demonstrate that the structurally lower unit of the KN (known as Sheopuri Gneiss) can be correlated to the L–GHS unit; this result strongly supports those models that correlate the KN to the Tethyan Sedimentary Sequence (TSS) and that suggest the merging of the South Tibetan Detachment System and the Main Central Thrust on the northern side of the KN. Moreover we speculate that, in this sector of the Himalayan chain, the most appropriate kinematic model able to explain the observed tectono-

This article has been accepted for publication and undergone full peer review but has not been through the copyediting, typesetting, pagination and proofreading process, which may lead to differences between this version and the Version of Record. Please cite this article as doi: 10.1111/jmg.12219

metamorphic architecture of the GHS is the duplexing model, or hybrid models which combine the duplexing model with another end-member model.

Key-words: Greater Himalayan Sequence, Himalaya, pseudosection modelling, *P–T* path, tectono-metamorphic architecture

INTRODUCTION

Being the archetype of collisional orogens, the Himalayan chain is considered as an exceptional natural laboratory for studying the tectono-metamorphic processes that occur during continental collision. The Greater Himalayan Sequence (GHS), which represents the exhumed metamorphic core of the Himalaya, is especially important for our understanding of orogenic processes. The GHS has long been considered as a coherent tectonic unit, sandwiched between the Lesser Himalayan Sequence (LHS) below and the Tethyan Sedimentary Sequence (TSS) above, from which it is separated by the Main Central Thrust (MCT; e.g. Gansser, 1964; Searle *et al*., 2008) and the South Tibetan Detachment System (STDS; Burchfield *et al*., 1992; Carosi *et al*., 1998; Kellett *et al*., 2010), respectively. However, since the discoveries of the first tectono-metamorphic discontinuities in some sectors of the GHS (e.g. Langtang: Inger & Harris, 1992; Reddy *et al*., 1993; Fraser *et al*., 2000; Kohn *et al*., 2004, 2005; Eastern Nepal: Goscombe *et al*., 2006; Groppo *et al*., 2009; Imayama *et al*., 2010, 2012), it is becoming more and more evident that the structural architecture of the GHS is much more complex than previously supposed (see Montomoli *et al*., 2015 and Larson *et al*., 2015 and references therein). It is now widely accepted that at least one, first-order, regional-scale tectono-metamorphic discontinuity (e.g. High Himalayan Discontinuity as defined by Montomoli *et al*., 2013 in western Nepal) characterizes the GHS, which is thus divided in two portions with different *P–T*–t evolution (e.g. Carosi *et al*., 2010; Larson *et al*., 2010; Yakymchuk & Godin, 2012; Montomoli *et al*., 2013). The scenario seems to be locally even more complex, with the possible existence of several tectono-metamorphic discontinuities (e.g. Larson & Cottle, 2014; Ambrose *et al*., 2015; Larson *et al*., 2015) within the GHS, which would therefore consist of multiple juxtaposed slices. The discovery of these discontinuities, often interpreted as in-sequence thrusts that were active prior to the MCT, has progressively weakened some of the most popular tectonic models used so far to explain the metamorphic and structural architecture of the Himalayan chain, such as the Channel flow model (Beaumont *et al*., 2001, 2004; Jamieson *et al*., 2004; Godin *et al*., 2006), and has led to the formulation of new "hybrid" models that combine elements of different end-member models (e.g. Cottle *et al*., 2015; He *et al*., 2015 and references therein).

The first recognised discontinuity within the GHS was located in the Langtang region, ~ 75 km north of Kathmandu in central Nepal (Inger & Harris, 1992). Due to relatively easy accessibility, the Langtang region was investigated in detail earlier than other Himalayan regions. Most of the studies performed in this area point to the existence of at least one metamorphic discontinuity, located ~ 7 km structurally above the MCT, which separates the GHS in two units (Inger & Harris, 1992; Reddy *et al*., 1993; Harris & Massey, 1994; Fraser *et al*., 2000; Kohn *et al*., 2004, 2005; Kohn, 2008). The upper part of the GHS unit mainly consists of sillimanite–bearing migmatites, which experienced lower peak–pressure conditions compared to the underlying kyanite–bearing rocks of the lower GHS unit (Inger & Harris, 1992, Fraser *et al*., 2000; Kohn *et al*., 2004, 2005). Geochronological data additionally suggest that melting in the upper GHS unit occurred earlier than

in the lower GHS unit (Kohn *et al*., 2004, 2005; Kohn, 2008; Corrie & Kohn, 2011). Compared to the Langtang region, which has been investigated in detail, the Gosainkund–Helambu region, extending for ~ 40 km to the south of Langtang toward the Kathmandu valley (Fig. 1), has been sparsely investigated (with the notable exception of Rai *et al*., 1998), remaining a "blank in the map" (see for example fig. 3b in Kohn, 2014). Although little studied, the Gosainkund–Helambu transect occupies a crucial position in the geological framework of the central Nepal Himalaya, connecting the Langtang region to the north with the Kathmandu Nappe (KN) to the south, whose tectonic interpretation is still largely debated in literature (e.g. He *et al*., 2015 and references therein). Studied since the '70–80s (Hagen, 1969; Stöcklin, 1980; Arita, 1983), the KN has been variously considered as part either of the LHS (e.g. Rai *et al*., 1998; Upreti & Le Fort, 1999; Hodges, 2000) or of the GHS (e.g. Johnson *et al*., 2001; Geherels *et al*., 2003; Robinson *et al*., 2003). More recently, the KN has been partially (e.g. Yin, 2006; Khanal *et al*., 2015) or completely (e.g. Webb *et al*., 2011) correlated to the TSS. Specifically, the interpretation of Khanal *et al.* (2015) implies that an intra–GHS thrust merges with the MCT on the northern side of the KN, whereas according to Webb *et al*. (2011) it is the STDS that merges with the MCT.

This paper focuses on the Gosainkund–Helambu region with the aim of reconstructing the structural and metamorphic architecture of the GHS along this poorly known transect. We addressed this problem via field-based investigations combined with the detailed petrological study (using the pseudosection approach) of several metapelite samples. In order to correlate the Gosainkund–Helambu transect with the Langtang section, the same approach is also applied on representative samples from the Langtang transect. We then compare our *P–T* estimates with those published by previous authors, using conventional and/or multi-equilibrium thermobarometry.

The obtained results allow us: (i) to constrain the *P–T* evolution experienced by the GHS rocks at different structural levels, both in the Gosainkund–Helambu and Langtang regions, and to correlate the two vertical sections; (ii) to confirm the existence of a tectono-metamorphic discontinuity within the GHS in the Langtang section that is located at a structural level too high to be intersected along the Gosainkund–Helambu section; (iii) to reconstruct the internal geometry of the leading edge of the GHS in a key area for understanding the development of Himalayan kinematic models.

GEOLOGICAL SETTING

The Greater Himalayan Sequence (GHS) comprises a Late Proterozoic to Cambrian metasedimentary sequence (Le Fort, 1975). From the lower to the upper structural levels, the following tectono-metamorphic units are generally recognised in the GHS: (i) medium– to high grade metasedimentary rocks and granitic orthogneisses, whose metamorphic grade increases structurally upward from medium to high (i.e. from the biotite to the sillimanite zones, through the garnet, staurolite and kyanite zones), with local anatexis (e.g. Pêcher, 1989; Goscombe *et al*., 2006; Kohn, 2008; Searle *et al*., 2008; Groppo *et al*., 2009, 2010; Mosca *et al*., 2012; Kohn, 2014); (ii) high-grade para– and orthogneisses (also called Higher Himalayan Crystallines: e.g. Pognante & Benna, 1993; Lombardo *et al*., 1993), often migmatitic, hosting networks and lens-shaped bodies of leucogranites (e.g. Visonà & Lombardo, 2002). These high-grade gneisses are characterized by a progressive decrease in peak–pressure structurally upward, marked by the progressive disappearance of garnet and kyanite and by

the appearance of cordierite and sillimanite (e.g. Pognante & Benna, 1993; Lombardo *et al*., 1993; Groppo *et al*., 2012, 2013).

The main lithological and tectono-metamorphic features of the Himalaya extend from west to east over distances of thousands of kilometres. Local perturbations of this general west-east attitude occur around major tectonic windows (e.g. Arun, Tamur and Tista windows in eastern Nepal and Sikkim: e.g. Goscombe *et al*., 2006 and references therein) and klippens (e.g. Kathmandu Nappe in central Nepal: e.g. Upreti & Le Fort, 1999; Johnson *et al*., 2001). North of Kathmandu in Central Nepal, one of these nappes is the synformal Kathmandu Nappe, exposing anchi-metamorphic to unmetamorphosed rocks (Johnson *et al*., 2001). The interpretation of this Nappe is controversial, as previously mentioned, and will be discussed in the following (see the Discussion section).

The study area is located north of the Kathmandu Nappe (KN), in the Langtang and Gosainkund–Helambu regions (Fig. 1a). The Langtang transect represents an ideal E-W cross section through the entire GHS, passing through both the STDS (close to the Nepal–Tibet boundary) to the east and the MCT (in the proximity of the junction between the Langtang and the Trisuli rivers) to the west. For this reason, and for its easy accessibility, the Langtang region has been investigated in detail since the ’90s, and its structural and lithological architecture is quite well known (Inger & Harris, 1992; Macfarlane *et al*., 1992; Macfarlane, 1993, 1995; Upreti, 1999; Fraser *et al*., 2000; Kohn *et al*., 2004, 2005; Pearson & DeCelles, 2005; Kohn, 2008). The Gosainkund–Helambu region occurs between the Langtang to the north and the Kathmandu Nappe to the south (Fig. 1b); it represents a link to connect lithological and structural features recognised in the Langtang region with those of the Kathmandu Nappe.

Tectono–stratigraphy and structural geometry of the studied area

At a regional scale, in central Nepal, the LHS is exposed below the GHS defining a roughly E–W striking anticlinorium (e.g. Pêcher, 1989). In the investigated area, the LHS consists of fine-grained phyllitic micaschists and mylonitic two-mica augen-gneisses (Syabru Bensi augen-gneiss in Takagi *et al*., 2003). The LHS rocks are tectonically thrust along the MCT by the GHS, mainly consisting of medium– to high-grade metapelites with intercalations of calc-silicate rocks and orthogneisses (Fig. 1b). In the Langtang region, the GHS and the underlying LHS display pervasive foliations mainly dipping NE to E and containing a pervasive dip-slip stretching lineation. Kinematic indicators (S–C fabrics, shear bands, rotated porphyroclasts and mica-fish) define a top–to–the–W/SW sense of shear across the MCT, with local evidences of later extensional top–to–the–NE movements near Syabru Bensi (see also Takagi *et al*., 2003). In the Gosainkund–Helambu region, the GHS foliation is E–W and is affected by folds with roughly WNW–ESE trending axes (see also Rai *et al*., 1998). South of Chisopani, Webb *et al.* (2011) and He *et al*. (2015) traced a S–dipping shear zone (Galchi Shear Zone: GSZ in Fig. 1b) with consistent top–to–the–north shear sense, which exposes the GHS rocks (also known as Sheopuri Gneiss, because they are exposed along the Sheopuri Range; Fig. 1b) in the footwall and the other units of the KN in the hanging wall (also known as Bhimpedi Group and Phulchauki Group).

Tectono-metamorphic architecture of the studied area

The results of previous petrological studies in both the Langtang and Gosainkund–Helambu regions are briefly summarized here and are more deeply discussed in the following sections. Inger & Harris (1992) first identified a metamorphic discontinuity in the Langtang region, based on a detailed thermobarometric study. This disconinuity separates a lower GHS unit, characterized by higher pressure at peak–*T* conditions (680–740°C, 8–10 kbar), from an upper GHS unit, which experienced lower pressure at peak–*T* conditions (730–790°C, 5.4–6.2 kbar) (Fig. 1b). These authors also confirmed that the metamorphic grade is inverted along the Langtang section, with the highest temperature samples clustered at the top of the section. In contrast, Macfarlane (1995) did not observe significant variations in peak–*T* up-section, but confirmed the decrease of peak–*P* towards structurally higher levels. Fraser *et al*. (2000) recognised two metamorphic discontinuities along the Langtang transect, thanks to the presence of pressure breaks detected using multi-equilibrium thermobarometry; the uppermost discontinuity recognised by Fraser *et al*. (2000) roughly coincides with that described by Inger & Harris (1992) (Fig. 1b). Kohn *et al*. (2004, 2005) and Kohn (2008) further refined the tectono-metamorphic architecture of the Langtang region combining detailed thermobarometric data (conventional thermobarometry and Zr–in–rutile thermometry) with geochronological data (Th–Pb on monazite) and suggested the existence of a main discontinuity (Langtang Thrust) separating an upper unit that experienced earlier melting at lower pressure conditions (20–18 Ma, 8.0–8.5 kbar) from a lower unit that experienced later melting at higher pressure conditions (*c.* 16–13 Ma, 10–12 kbar). The Langtang thrust, as defined by Kohn *et al*. (2004, 2005) and Kohn (2008), is located a few km structurally higher than the Inger & Harris (1992) discontinuity (Fig. 1b). In the Gosainkund–Helambu transect, Rai *et al*. (1998) combined conventional and multi-equilibrium thermobarometric methods and constrained peak *P*–*T* conditions in the range 600–750°C, 6–9 kbar.

PETROGRAPHY AND MINERAL CHEMISTRY

For both the Gosainkund–Helambu and Langtang transects, the studied samples are described from lower to higher structural levels (Fig. 1c) and are therefore reported in the same order in all relevant figures and tables. The most representative microstructures are reported in Figs 2–4 & S1, mineral chemical data are reported in Figs 5–6 and Tables 2 & S1–S3, and crystallization–deformation relations are summarized in Fig. S2. In the following, major emphasis is given to the petrographic description of the samples from the Gosainkund–Helambu transect, for which very few data are reported in the literature, whereas the microstructural features of the samples from the Langtang transect are only briefly summarized. Mineral abbreviations are according to Whitney & Evans (2010) (Als = aluminosilicate; Wm = white mica). Note that samples 14–03, 14–25b, 14–24 and 14–08a from the Langtang section have been collected close to samples LT01–74/75, LT01–29b, LT01–27b and LT01–6c of Kohn (2008), respectively.

Gosaikund–Helambu section

Sample 14–27a: Two-mica graphitic phyllite, with porphyroblastic Grt

This sample is a fine-grained rock consisting of white mica, quartz, biotite, chlorite, garnet, plagioclase, minor epidote and accessory graphite, ilmenite and tourmaline. It is characterized by a well-developed biotite + white mica + graphite foliation (S_m; Fig. 3a), which is derived from the transposition of an older schistosity (S_{m-1}) defined by the preferred orientation of chlorite, biotite

and white mica (+ plagioclase and ilmenite) still preserved in microlithons (Fig.3b). Discontinuous lenses, few mm-thick, rich in quartz and plagioclase are parallel to the main foliation.

Garnet porphyroblasts (up to 2 mm in diameter) are dispersed in the matrix; they are partly wrapped by the main foliation, and include a rotated internal foliation (i.e. snow-ball microstructure, Fig. 3a) defined by the alignment of quartz, chlorite, ilmenite and graphite inclusions. Small anhedral plagioclase crystals occur both in the microlithons and in the S_m. Late biotite, white mica and chlorite occur as small flakes statically overgrowing S_m (Fig. 3b). Late chlorite locally replaces garnet at the rims, as well as the late biotite flakes. Sub-millimetric idioblastic crystals of epidote are dispersed in the matrix. Fine-grained graphite is locally abundant in the micaceous domains.

Sample 14–44a: Wm + Bt + Ky micaschist, with porphyroblastic Grt

This sample is a medium-grained two-mica schist consisting of white mica, quartz, plagioclase, biotite, garnet, minor kyanite and accessory graphite, rutile and ilmenite. It shows a compositional layering (Fig. 2) defined by discontinuous quartz + plagioclase domains alternated with continuous pluri-mm thick layers consisting of white mica + biotite + garnet + rare kyanite. The main foliation (S_m), parallel to the compositional layering, is defined by the alignment of large flakes of both white mica and biotite; locally, white mica flakes up to 1 mm in length statically overgrow the S_m fabric.

Garnet is up to 1 mm in diameter; it occurs as idioblasts showing equilibrium relationships with white mica and biotite that define the S_m (Fig. 3c). The garnet core is crowded with small inclusions of quartz, biotite, rutile and ilmenite, whereas the rim is almost free of inclusions; the transition between garnet core and rim is marked by the presence of polymineralic inclusions, up to 50 µm in width (Fig. 3d), interpreted as nanogranites (Cesare *et al*., 2009) and consisting of feldspar + quartz + chlorite + zircon. The occurrence of nanogranites thus implies that garnet rim has a peritectic nature. Plagioclase is abundant in the leucocratic layers. Kyanite is rare and occurs as crystals in the micaceous layers (Fig. 3d). Among accessory phases, graphite is oriented parallel to S_m.

Sample 14–61b: Bt + Wm micaschist, with porphyroblastic Grt

This sample is a medium-grained micaschist consisting of plagioclase, quartz, white mica, biotite, K-feldspar, garnet, and accessory rutile and ilmenite. The well-developed foliation (S_m) is defined by the preferred orientation of biotite and minor white mica (Fig. 3e), concentrated in continuous mm-thick layers, alternated with pluri-mm quartz + plagioclase + K-feldspar ± biotite leucocratic domains. The main foliation S_m wraps around large garnet porphyroblasts (up to 6 mm in diameter) (Fig. 3e,f). Locally, late white mica flakes overgrow the S_m.

Garnet porphyroblasts host abundant inclusions of quartz, biotite, plagioclase, white mica and ilmenite, equally distributed from core to rim; locally, garnet has the typical appearance of a peritectic phase, growing around large polymineralic inclusions consisting of rounded and corroded white mica, plagioclase and quartz (Fig. 3f). K-feldspar is widespread in the matrix and is partially replaced by plagioclase at its rim. Plagioclase in the matrix occurs as large granoblastic crystals, up to 5 mm in length locally showing anti-perthitic structures. Accessory rutile is rare and is replaced by ilmenite; ilmenite occurs both as inclusion in garnet and in the matrix.

Sample 14–71: Wm + Bt + Grt + Sil gneissic micaschist

This sample is a medium-grained gneissic micaschist, consisting of quartz, white mica, biotite, plagioclase, garnet, minor sillimanite, and accessory ilmenite, rutile and tourmaline. The main foliation (S_m) is defined by the alignment of biotite and white mica, concentrated in mm-thick layers, alternated with discontinuous quartz + plagioclase + minor biotite layers (Figs 2 & 3g).

Garnet porphyroblasts, up to 2 mm in diameter, are enveloped by the main foliation, although the rim shows equilibrium relationships with both biotite and white mica of the S_m (Fig. 3g). Garnet is microstructurally zoned, with the core crowded with monomineralic inclusions (quartz, plagioclase, biotite, ilmenite), whereas the rim is almost inclusion-free. The transition from core to rim is marked by the presence of few quartz + plagioclase + zircon + rutile + chlorite nanogranites, up to 30 µm in width (i.e. garnet rim has a peritectic nature). Biotite and white mica define the main foliation. Large white mica flakes (up to 3 mm) overgrow the S_m and include quartz and rare, randomly oriented, fine-grained sillimanite. Among accessory phases, ilmenite occurs both in the garnet and in the matrix.

Sample 14–52: Bt + Sil + Ky fine-grained gneiss, with porphyroblastic Grt

This sample is a fine-grained gneiss consisting of quartz, biotite, plagioclase, sillimanite, garnet, minor kyanite and accessory ilmenite. It has a banded structure, defined by quartz + biotite + plagioclase ± kyanite ± garnet ± sillimanite mesocratic domains, alternating with sillimanite + quartz ± plagioclase ± biotite leucocratic layers (Fig. 2). The leucocratic domains are continuous and up to 1 mm thick, whereas the mesocratic biotite–rich layers are thicker (up to 1 cm). The main foliation (S_m) is parallel to the compositional layering and is defined by the alignment of biotite lepidoblasts and, locally, by sillimanite (Fig. 3h,i).

Garnet is rare but, where observed, it is up to 1.5 mm in diameter. It is wrapped by the main foliation (Fig. 3h) but rounded bulges are observed locally. Garnet includes quartz, biotite, white mica and very small crystals of kyanite at its rim. Kyanite is scarce but, in addition to occurring as small inclusions in garnet, it is also found as isolated relicts in the matrix, replaced by plagioclase (Fig. 3h). Plagioclase is more abundant in the biotite–rich domains; it locally includes quartz and minor biotite. Sillimanite is fine-grained and prismatic; it mainly occurs in the leucocratic layers (Fig. 3i) associated with minor biotite, plagioclase and quartz aggregates. Ilmenite is scarce and concentrated in the biotite–rich domains.

Mineral chemistry of the samples from the Gosainkund–Helambu section

Garnet is strongly zoned in sample 14–27a (XMn and XCa decrease toward the rim, whereas both XMg and XFe increase), while it is homogeneous in composition in samples 14–44a, 14–61b and 14–71. In garnet from sample 14–52, a slight decrease in XMg balanced by an increase in XMn toward the rim likely reflects diffusional homogenization at high temperatures.

Biotite is internally homogeneous in composition in sample 14–27a, where it defines both S_{m-1} and S_m. In samples 14–44a, 14–71 and 14–52 biotite included in garnet has lower Ti content (sample 14–44a and 14–52) and/or higher XMg (sample 14–44a and 14–71) with respect to the biotite defining S_m. Opposite to the majority of the samples, in sample 14–61b biotite inclusions in garnet have lower XMg than the biotite in the matrix, while Ti content is homogeneous. In sample 14–27a the different white mica generations have different compositions, with Si content increasing

in lepidoblasts defining the S_m (Na content is quite homogeneous). In samples 14–44a and 14–61b white mica included in garnet and the cores of white mica defining the S_m have higher Si content compared to the rims of white mica in the matrix. In samples 14–71 and 14–52 white mica is homogeneous in composition.

Plagioclase is slightly zoned in all the samples, with anorthite content generally increasing toward the rim, except in sample 14–27a, where XAn decreases from core to rim; plagioclase inclusions in garnet are more calcic in composition (samples 14–61b and 14–71) with respect to plagioclase in the matrix. Where present, K-feldspar is slightly zoned, with orthoclase content increasing toward the rim (sample 14–61b).

Chlorite in sample 14–27a from the different microstructural sites shows only slight differences in composition: chlorite included in garnet has lower XMg than chlorite defining S_{m-1} and replacing biotite and garnet. All chlorites are ripidolite (and minor pycnochlorite) according to Hey (1954).

Epidote in sample 14–27a varies in composition from Zo_{40} to Zo_{55} [Zo component defined as: $Al/(Al+Fe^{+3})$].

Mineral chemistry data are summarized in Table 2a.

Langtang section

Samples 14–03, 14–25b and 14–24: Wm + Bt + Grt ± St ± Ky gneissic micaschists

These samples are medium- to coarse-grained gneissic micaschists, consisting of white mica, biotite, garnet, plagioclase, quartz, ± kyanite ± staurolite (in samples 14–25b and 14–24) and accessory rutile, ilmenite and tourmaline. The main planar foliation (S_m) is defined by mm-thick white mica + biotite layers alternated with pluri-mm thick discontinuous quartz domains (Fig. 4a,c,e). White mica and biotite occur as large flakes (up to 5 mm in length) oriented to define the main foliation; locally, a later generation of white mica statically overgrows the S_m fabric.

Garnet porphyroblasts (up to 2 mm in diameter) are in equilibrium with both white mica and biotite and are mainly concentrated in the micaceous layers. The larger garnet crystals are microstructurally zoned, with the core and mantle crowded with inclusions (quartz, biotite, rutile, ilmenite ± plagioclase), whereas the rim is almost free of inclusions (Fig. 4b,f). The transition between garnet core and rim is marked by the presence of small polymineralic inclusions, up to 50 µm in width, interpreted as nanogranites and mainly consisting of quartz ± albite ± feldspar ± biotite ± epidote ± rutile ± zircon ± apatite ± ilmenite (Fig. 4b,f) (i.e. garnet rim is peritectic).

Kyanite occurs as large idioblasts mainly oriented parallel to S_m or overgrowing it (Fig. 4c,e). Staurolite generally overgrows the S_m and replaces kyanite at its rim (Fig. 4c,d,g).

Plagioclase is rare in sample 14–03, where it locally overgrows the S_m and includes biotite and quartz; it is abundant in samples 14–25b and 14–24 where it occurs as subhedral crystals and it locally includes quartz. Small and rare fibrolitic sillimanite replaces both garnet and white mica rims

in samples 14–03 and 14–25b. In all the samples rutile and ilmenite occur both as inclusions in garnet and in the matrix; ilmenite often replaces rutile at its rim.

Sample 14–08: Bt + Sil + Grt migmatite

This sample is a medium-grained migmatite, consisting of quartz, plagioclase, K-feldspar, biotite, sillimanite and garnet, late white mica, and accessory ilmenite and graphite. It is characterized by a banded structure (Figs 2 & 4h), defined by biotite + sillimanite + quartz ± garnet mm-thick mesocratic domains alternating with quartz + plagioclase + K-feldspar ± sillimanite ± garnet pluri-mm leucocratic layers. The main foliation (S_m) is parallel to the compositional layering and is defined by the preferred orientation of biotite lepidoblasts and fibrolitic sillimanite.

Garnet porphyroblasts are scarce but, where present, they contain large polymineralic inclusions of biotite + quartz ± plagioclase and biotite + quartz ± zircon ± apatite ± plagioclase ± feldspar ± white mica nanogranites, up to 100 μm in diameter (Fig. 4h), suggesting that it has a peritectic nature. Biotite in the matrix mainly defines the S_m, which is locally overgrown by large flakes of white mica. K-feldspar and plagioclase are mainly concentrated in the leucocratic domains; large crystals of plagioclase (up to 5 mm) contain vermicular inclusions of quartz. Mirmeckitic structures occur at the interface between K-feldspar and plagioclase.

The mesocratic domains are characterized by the occurrence of biotite + quartz + sillimanite + plagioclase symplectites developed at the expenses of K-feldspar and garnet (Fig. 4i) and of white mica + quartz + plagioclase symplectites developed at the expense of K-feldspar. These symplectitic microstructures are generally interpreted, in migmatites, as related to the late interactions between solids and melt (i.e. back-reactions) during final melt crystallization (e.g. Waters, 2001; Cenki *et al*., 2002; Kriegsman & Álvarez-Valero, 2010). Further evidence for the presence of former melt is the local occurrence of thin films of quartz and/or feldspar, occupying interstitial positions, and interpreted as "melt pseudomorphs" (according to the definition of Holness & Clemens, 1999; Holness & Sawyer, 2008) (Fig. 4i). Late, large flakes of white mica statically overgrow sillimanite defining the S_m. Accessory ilmenite is often associated with white mica.

Mineral chemistry of the samples from the Langtang section

Garnet is slightly zoned in samples 14–03, 14–25b and 14–24 (XMn and XCa decrease from core to rim whereas both XMg and XFe increase) whereas it is quite homogeneous in sample 14–08a. In all the samples biotite inclusions in garnet have, on average, higher XMg and lower Ti contents than that in the matrix. White mica is internally homogeneous in composition in all the samples. Plagioclase included in garnet has usually higher anorthite content than that in the matrix (except in sample 14–25b), which is locally zoned (XAn increasing toward the rim in samples 14–03 and 14–24; XAn decreasing toward the rim in sample 14–08a). K-feldspar in sample 14–08a is homogeneous in composition. Staurolite in samples 14–25b and 14–24 is slightly zoned, with XMg decreasing toward the rim. Mineral chemistry data are summarized in Table 2b.

THERMODYNAMIC MODELLING

The *P–T* evolution of the nine metapelite samples has been constrained using the pseudosection approach; for three samples (14–27a, 14–03 and 14–25b), two pseudosections have been calculated, considering the fractionation effects on the bulk composition due to the growth of zoned garnet

porphyroblasts. A total of 12 *P–T* pseudosections have been therefore modelled. In the following, major emphasis is given to the samples from the Gosainkund–Helambu transect, for which very few *P–T* constraints are reported in the literature (Rai *et al*., 1998). The results obtained for the samples from the Langtang transect are also discussed, but the pseudosections are given as Figs S3–S6. Details on the calculation (i.e. model system, solution models) are given in Appendix S1.

Most of the studied samples are two-mica schists lacking microstructural evidence of partial melting, except for the presence of nanogranites included in garnet rim (i.e. samples: 14–03, 14–24, 14–25b, 14–44a, 14–71). These two-mica schists have been therefore modelled at both sub-solidus and supra-solidus conditions. H_2O has been considered as an excess fluid phase at sub-solidus conditions. The position of the solidus and the supra-solidus topologies were calculated at H_2O-saturated conditions, i.e. using an amount of H_2O sufficient to saturate the system at *P–T* conditions immediately below the solidus.

For those samples with microstructures indicative of partial melting (i.e. samples 14–08a, 14–61b) a different approach was used. The *P–T* pseudosection modelling of migmatitic rocks, in fact, is complicated by the possibility that the system had experienced one or more episodes of melt loss and that the actually measured bulk rock composition is somewhat different from that of the protolith. Since in migmatitic rocks the observed mineral assemblages and modes are those corresponding to the final crystallization of the melt (i.e. at the *P–T* conditions where the *P–T* trajectory intersects the solidus of the system), the measured bulk composition (and H_2O content) can be used to model the *P–T* conditions of melt crystallization. Furthermore, because it is unlikely that melt loss occurred during crystallization (i.e. at decreasing temperature), the measured bulk composition can be also used to model the retrograde portion of the metamorphic evolution, from peak–*T* to the final melt crystallization (e.g. Clarke *et al*., 2007; Indares *et al*., 2008; Groppo *et al*., 2012 for further details). In this case, the pseudosections have been therefore calculated using the measured bulk compositions and a H_2O content derived from the modal proportion of biotite (± white mica) (see Appendix S1).

For all the samples, prograde and peak *P–T* conditions have been constrained based on the stability field of the observed prograde and peak mineral assemblages, combined with garnet compositional isopleths. Biotite compositional isopleths have been additionally used for the migmatitic sample 14–08, because garnet composition has been likely modified by diffusion. The retrograde portion of the *P–T* trajectories is generally less well constrained than the prograde one; *P–T* constraints are given by the inferred stability fields of the retrograde assemblages. For the migmatitic sample 14–08 further constraints are given by the intersection between the mineral isomodes and the solidus.

Gosainkund–Helambu section

Prograde and peak P–T conditions

All the pseudosections calculated for the metapelites from the Gosainkund–Helambu section are dominated by tri–, quadri– and quini– variant fields. The results of pseudosection modelling allow the following prograde and peak *P–T* conditions to be constrained:

Sample 14–27a – The pseudosection for the unfractionated composition (Fig. 7a) gives information about the mineral assemblage stable during the prograde growth of garnet core, represented by the relatively large Bt + Qz + Pl + Ms + Grt + Ilm + H_2O field, which occurs at >500°C and <12 kbar; the fractionated pseudosection (Fig. 7c) predicts the growth of garnet rim in the same quini-variant field. The earlier S_{m-1} mineral assemblage is modelled by the tri-variant Bt + Chl + Qz + Pl + Ms + Grt + Zo + Ilm + H_2O field, at <510°C, 4.0<P<7.5 kbar. Garnet core compositional isopleths (XMg=0.03–0.04; XCa=0.23–0.25; XMn=0.12–0.15) give 510–540°C and 5.3–5.7 kbar (Fig. 7b), whereas garnet rim composition (XMg=0.05–0.06; XCa=0.19–0.22; XMn=0.05–0.07) constrains peak *P–T* conditions of 570–620°C, 6.7–8.2 kbar (Fig. 7c; Table 3).

Sample 14–44a – The equilibrium assemblage, consisting of garnet, biotite, white mica, kyanite, quartz, plagioclase ± rutile ± ilmenite, is modelled by the quini-variant Bt + Qz + Pl + Ms + Grt + Ky + H_2O/L fields at >640°C, >6.4 kbar (Fig. 8a). Further constraints are given by garnet compositional isopleths (XMg=0.16–0.18; XCa=0.04–0.05; XMn=0.05–0.06) that suggest peak *P–T* conditions of 700–750°C, 8.6–10.0 kbar (Fig. 8b; Table 3). The H_2O-saturated solidus is located at 670–700°C (Fig. 8c), implying that the peak assemblage was stable in the presence of very low amounts of melt (< 2 vol. %); this is in agreement with the observed peritectic nature of garnet.

Sample 14–61b – The pseudosection shows that the first melt production occurs at 720–750 °C, > 8 kbar (Fig. 9a). A low amount of melt (< 2.4 vol. %) is predicted in the Bt + Qz + Pl + Kfs + Ms + Grt + L field, located in between the solidus and the Wm-out reaction curve, whereas up to 8.0 vol. % of melt is produced through the complete white mica dehydration melting. The equilibrium assemblage, consisting of garnet, biotite, white mica, K-feldspar and plagioclase ± melt, is modelled by the large quini-variant melt-absent Bt + Pl + Qz + Grt + Kfs + Ms field and by the narrow quadri-variant melt-bearing Bt + Qz + Pl + Grt + Kfs + Ms + L field (Fig. 9a). Further constraints are given by garnet compositional isopleths (XMg=0.12–0.13; XCa=0.02–0.03; XMn=0.03–0.04), which indicate equilibration temperatures of 730–750°C and pressures of 9.4–11.3 kbar (Fig. 9b; Table 3). The stability field of peak mineral assemblage is thus located across the solidus, but still inside the white mica stability field, in agreement with microstructural observations, which suggest that partial melting was incipient and that white mica is still stable.

Sample 14–71 – The equilibrium assemblage, consisting of garnet, biotite, white mica, plagioclase, quartz, ilmenite ± rutile, is modelled by the Bt + Qz + Pl + Ms + Grt + H_2O/L ± Ilm ± Rt field, located at 500–760°C and 3–15 kbar (Fig. 10a). Garnet compositional isopleths (XMg=0.10–0.11; XCa=0.03–0.04; XMn=0.04) constrain the growth of the equilibrium assemblage at 710<T<750°C and 8.5<P<10.8 kbar (Fig. 10b; Table 3). Peak *P–T* conditions lie just above the H_2O-saturated solidus (Fig. 10c); the predicted amount of melt at peak *P–T* conditions is nevertheless very low (< 1.5 vol%).

Sample 14–52 – The maximum values of XMg measured in garnet core have been considered to constrain peak *P–T* conditions. Garnet includes biotite, quartz, minor kyanite and very minor white mica; this assemblage is modelled by the quini-variant field Bt + Pl + Ms + Grt + Ky + Qz + H_2O at >650°C and 8.7<P<11.7 kbar (Fig. 11a). Further constraints are given by garnet core compositional isopleths (XMg=0.20–0.21; XCa=0.03; XMn=0.11–0.12) that point to peak conditions of 720<T<760°C and 9.0<P<10.0 kbar (Fig. 11b; Table 3). The modelled XMn isopleths predict lower XMn at these *P–T*

conditions (XMn=0.06–0.07), further supporting that garnet composition could have been modified by diffusional homogenization (see the Mineral chemistry section).

Retrograde evolution

The retrograde portion of the *P–T* path is less tightly constrained than the prograde one for all the studied samples. A cooling and decompression retrograde path can be nevertheless inferred for all the samples, basing on the following observations:

Sample 14–27a – The local occurrence of biotite, white mica and chlorite statically overgrowing S_m suggests a retrograde path dominated by cooling and decompression toward the chlorite stability field (Fig. 7d). These observations are in agreement with the calculated isomodes for biotite and chlorite (not reported in the figures), showing that both these minerals can grow during cooling and decompression.

Sample 14–44a – A cooling and decompression retrograde path is compatible with the observed zoning in plagioclase, that is enriched in anorthite component toward the rim, as predicted by the plagioclase compositional isopleths (not reported in the figures).

Sample 14–61b – Any cooling and decompression retrograde path would imply the entrance in the kyanite (or sillimanite) stability field (Fig. 9c). Neither kyanite nor sillimanite are observed in metapelite 14–61b; however, the calculated isomodes predict that their modal amount is lower than 0.1 vol. %.

Sample 14–71 – The occurrence of rare sillimanite suggests that the retrograde *P–T* path enters the sillimanite stability field (Fig. 10c).

Sample 14–52 – Garnet porphyroblasts are wrapped by the main foliation defined by oriented biotite and sillimanite, with additional plagioclase and quartz in equilibrium with them. This assemblage is modelled by the large esa-variant field Bt + Pl + Grt + Sil + Qz + H_2O at >670°C and < 10.1 kbar (Fig. 11c). The observed slight zoning of plagioclase is further consistent with decompression associated with cooling.

Langtang section

Prograde and peak P–T conditions

Sample 14–03 – The unfractionated pseudosection (Fig. S3a) gives information about the mineral assemblage stable during the growth of garnet core that includes biotite, quartz, rutile, ilmenite and white mica. This assemblage is represented by the quini-variant Bt + Qz + Pl + Ms + Grt + Rt + H_2O (± Ilm) fields at >600°C and >7 kbar; plagioclase has not been observed as inclusions in garnet perhaps because it was totally consumed during prograde metamorphic reactions. Further constraints on the *P–T* conditions at which garnet core grew are given by its compositional isopleths (XMg=0.14–0.15; XCa=0.07; XMn=0.06–0.07), which give 650–670°C and 7.4–8.8 kbar (Fig. S3b). The topology of the fractionated pseudosection (Fig. S3c), almost identical to the previous one, suggests that fractionation effects were minimal. The garnet rim is in equilibrium with biotite, white mica, plagioclase, quartz and rutile: this assemblage is modelled by the quini-variant fields Bt + Qz + Pl + Ms + Grt + Rt + H_2O/L, at >7 kbar and >600°C. Compositional isopleths (XMg=0.17–0.18; XCa=0.05–0.06; XMn=0.04–0.05) constrain the growth of garnet rim at 710–730°C and 9.6–11.0 kbar (Fig. S3c; Table 3). Garnet core grew at sub-solidus conditions, whereas the first melt appears in the range 670–700°C, i.e. during the growth of garnet rim (Fig. S3d), coherently with its peritectic nature. The amount of melt produced at peak *P–T* conditions is very low, i.e. < 1 vol. %.

Samples 14–25b and 14–24 – Although the pseudosections calculated for these samples are very similar (Figs S4a & S5a), the preserved growth zoning of garnet in sample 14–25b allows its prograde evolution to be constrained, whereas only peak *P–T* conditions can be inferred from sample 14–24. In sample 14–25b the prograde mineral assemblage stable during the growth of garnet core is represented by white mica, biotite, quartz, plagioclase, rutile and ilmenite. This assemblage is modelled by the quadri- and quini-variant Bt + Qz + Pl + Ms + Grt + Rt + H_2O ± Ilm fields at >600°C and >7.8 kbar. Compositional isopleths for garnet core (XMg=0.13; XCa=0.04; XMn=0.05) further constrain its growth at 630<T<640°C and 8.0<P<8.2 kbar, very close to the kyanite-in curve (Fig. S4b). The garnet rim is in equilibrium with biotite, white mica, kyanite, plagioclase, quartz and rutile; this assemblage is modelled by the relatively narrow quadri-variant Bt + Qz + Pl + Ms + Grt + Ky + Rt + H_2O/L fields, at >640°C and >7.8 kbar. Compositional isopleths of garnet rim (XMg=0.15; XCa=0.03; XMn=0.04) intersect perfectly in this field and constrain the growth of the peak assemblage at 715–725°C, 9.7–10.0 kbar (Fig. S4b; Table 3). As concerning sample 14–24, the equilibrium assemblage, consisting of quartz, garnet, biotite, white mica, kyanite, plagioclase and rutile, is modelled by a quadri-variant field at >640°C and >7 kbar. Compositional isopleths of garnet (XMg=0.14–0.16; XCa=0.04–0.05; XMn=0.04–0.05) constrain peak *P–T* conditions at 725<T<760°C and 9.7<P<10.8 kbar (Fig. S5b; Table 3). For both the samples, the peak *P-T* conditions lie just above the H_2O-saturated solidus (Figs S4c & S5c), thus explaining the peritectic nature of garnet rim. The amount of melt produced at peak *P-T* conditions is very low (< 2 vol. % and < 1 vol. %, respectively).

Sample 14V08a – The equilibrium assemblage, consisting of garnet, biotite, K-feldspar, plagioclase, sillimanite, quartz, ilmenite and melt, is modelled by a large quadri-variant field at 650<T<850°C and <9 kbar. Further constraints are given by the compositional isopleths of garnet and biotite. Garnet is quite homogeneous in composition, reflecting diffusional homogenization effects at high temperatures; a slight increase in calcium is observed toward the rim (XCa=0.04–0.05). This Ca increase can be interpreted as related to the crossing of the muscovite dehydration melting curve, along a nearly isobaric *P–T* trajectory at about 7–8 kbar (Fig. S6b). The maximum XMg of garnet (XMg=0.12) constrains the equilibration temperatures at ~ 760°C; slightly higher temperatures (760–800°C) are suggested by XMg isopleths of biotite included in garnet (XMg=0.38; Fig. S6b; Table 3). Due to possible compositional reset during cooling, the obtained temperatures should be considered as “minimum” estimates.

Retrograde evolution

The retrograde portion of the path is generally less well constrained than the prograde one. A cooling and decompression retrograde path can be nevertheless inferred for all the samples, basing on the following observations:

Sample 14–03 – The occurrence of rare sillimanite at the rim of garnet and white mica qualitatively constrains the retrograde path at *P–T* conditions below the kyanite–sillimanite transition.

Samples 14–25b and 14–24 – The retrograde evolution is tightly constrained at 590-650°C, < 8.0 kbar by the growth of staurolite replacing kyanite and by the rare occurrence of fibrolitic sillimanite replacing garnet rim.

Sample 14–08 – The retrograde evolution of this sample is inferred using the calculated isomodes for all mineras. The intersection between the modelled isomodes and the solidus constrain

the *P–T* conditions for the final melt crystallization at ~ 700°C, 6 kbar (Fig. S6c). Back-reactions between solids and melt during melt crystallization are responsible for the formation of symplectitic intergrowths between: (i) biotite + sillimanite + plagioclase + quartz (according to the back-reaction: Grt + Kfs + L $\rightarrow$ Bt + Als + Pl + Qz at higher T), and (ii) white mica + plagioclase + quartz (according to the back-reaction: Kfs + Als + Grt + L $\rightarrow$ Wm + Pl + Qz at lower temperature, i.e. at the solidus).

DISCUSSION

Metamorphic evolution along the Langtang section

The results of phase petrology modelling of selected metapelite samples from the Langtang section indicate the occurrence of two distinct tectono-metamorphic units, characterized by different chemical zoning patterns in garnet, different *P–T* paths and *T/*depth ratios.

The structurally lower unit (Lower Greater Himalayan Sequence: L–GHS) mainly consists of medium-grade, garnet ± kyanite ± staurolite –bearing two-mica schists, lacking evidence of partial melting at the outcrop scale. These lithologies are characterized by garnet zoning profiles from strongly zoned to slightly zoned. The structurally lower samples preserve evidence of their prograde history, characterized by an increase in *P-T* up to peak metamorphic conditions of 720 ± 10 °C, 10.3 ± 0.7 kbar, in the kyanite stability field (Fig. 12a). Similar peak *P–T* conditions are inferred for the structurally higher sample, which does not preserve evidence of its prograde evolution and is characterized by garnet homogeneous in composition. These peak *P–T* conditions correspond to a *T/*depth ratio of 22 ± 1 °C km^{-1} (assuming an average lithostatic pressure gradient of 0.3 kbar km^{-1}) (Table 3). Furthermore, peak metamorphic conditions of these three samples lie just above the H_2O-saturated solidus; the predicted amount of melt at these *P–T* conditions is very low and is in agreement with the occurrence of nanogranites at the transition between garnet core and garnet rim. The retrograde evolution of these metapelites is characterized by cooling and decompression in the staurolite stability field (Fig. 12a).

The structurally higher unit (Upper Greater Himalayan Sequence: U–GHS) mainly consists of high grade migmatites showing widespread evidence of partial melting at the outcrop scale. These metapelitic migmatites are characterized by chemically homogeneous minerals and well-equilibrated assemblages and do not preserve relicts of their prograde history. Peak metamorphic conditions of 780 ± 20 °C, 7.8 ± 0.8 kbar (i.e. temperature higher than the white mica dehydration-melting curve) have been inferred (Fig. 12a), in agreement with field and microstructural observations which indicate a widespread anatexis. Melt crystallization along the retrograde path occurred well within the sillimanite stability field (Fig. 12a). Peak *P–T* conditions inferred for the U–GHS unit correspond to a *T/*depth ratio of 31 ± 4°C km^{-1} (Table 3).

The different *P–T* trajectories and *T/*depth ratios obtained for the studied metapelites suggest the occurrence of a metamorphic discontinuity separating the L–GHS from the U–GHS, located ~ 5.5 km structurally above the MCT and marked by a significant decrease of peak–*P* conditions, corresponding to an abrupt increase in the *T/*depth ratios (Fig. 13; Table 3).

These results are consistent with those obtained from the Langtang section by previous authors, using different petrological approaches. Inger & Harris (1992) first documented the increase in peak–*T* and the decrease in peak–*P* up-section along the Langtang transect, using multi-equilibrium thermobarometry applied on a large number of metapelite samples. However, they attributed the two populations of peak–*P* to a diachronous metamorphism between the kyanite and the sillimanite zones, rather than to the presence of a cryptic discontinuity. Reddy *et al*. (1993) also argued for the presence of a tectonic break between kyanite– and sillimanite–grade rocks, combining geochemical, structural and textural arguments, but they did not provide *P*–*T* data. Fraser *et al*. (2000), using the Average–PT (ΔPT) approach, recognized the presence of two distinct, possibly duplicated units, basing on different peak–*P* estimates.

More recent estimates of peak *P*–*T* conditions from the Langtang section are those by Kohn *et al*. (2004, 2005) and Kohn (2004, 2008): conventional thermobarometry and trace element thermometry were applied on a significant number of metapelite samples and provided detailed *P*–*T* constraints for the metamorphic peak at different structural levels. Thermobarometric data mostly referred to the peak mineral assemblages and did not allow the reconstruction of the whole *P*–*T* evolution of the studied samples; however, geochronological data combined with *P*–*T* estimates were interpreted to indicate a *P*–*T*–t discontinuity along the Langtang section. This discontinuity (Langtang Thrust: Kohn *et al*., 2005) separates the GHS in two units, characterized by different peak *P*–*T* conditions and by different *P*–*T*–t histories: partial melting (and melt crystallization) occurred earlier in the U–GHS (20–18 Ma) than in the L–GHS (16–13 Ma), consistently with in-sequence thrusting of the U–GHS over the L–GHS.

Our peak *P*–*T* conditions (as well as garnet zoning patterns) obtained for samples 14–03, 14–25b, 14–24 and 14–08a using the pseudosection approach are in very good agreement with those obtained by Kohn *et al*. (2004, 2005) and Kohn (2004, 2008) on samples from the same structural levels (LT01–74/75, LT01–29b, LT01–27b and LT01–6c, respectively) using the conventional thermobarometry approach, thus confirming the complementary nature of the two methods (Tables 3 & S4). The pseudosection approach has the advantage of allowing the reconstruction of the prograde and/or retrograde *P*–*T* evolution of the studied samples, which can outline the differences and similarities of *P*–*T* paths in a set of samples otherwise only grouped by coherent peak *P*–*T* conditions. *T*/depth ratios calculated for the Kohn (2008) original data are also consistent with those obtained from our samples, and highlight the existence of two different *T*/depth ratio populations of 21 ± 3 °C km^{-1} and 28 ± 4 °C km^{-1} in the L–GHS (ZG1 and ZG2 in Kohn, 2008) and U–GHS (ZG3 and ZG4 in Kohn, 2008), respectively (Fig. 13 and Table S4). The metamorphic discontinuity marked by the abrupt increase in the *T*/depth ratio up-section inferred from our own data and from those of Kohn (2008) roughly coincides with the geochronological discontinuity marked by the increase in ages up-section as reported in Kohn *et al*. (2005) and Kohn (2008). There may be minor mismatch between the metamorphic and the geochronological discontinuities (see Fig. 1b), mainly related to the attribution of sample LT01–10 of Kohn (2008) to the upper vs. lower GHS unit. We therefore suggest that *T*/depth ratio is a useful parameter, alternative and/or complementary to the geochronological constraints, for the identification of metamorphic discontinuities within the GHS (see also Groppo *et al*., 2009).

Metamorphic evolution along the Gosainkund–Helambu section

Among the studied samples from the Gosainkund–Helambu section, the structurally lowest sample belongs to the LHS (structural distance below MCT < 1 km). The metamorphic evolution inferred for this metapelite consists of a narrow hairpin *P–T* path characterized by a prograde increase in both temperature and pressure followed by decompression associated with cooling (Fig. 12b). Garnet porphyroblasts show a well preserved growth zoning. Peak conditions experienced by sample 14–27a define a *T/*depth ratio of 24 ± 3 °C km^{-1} (Table 3). These results are consistent with those reported by previous authors (see for example sample LT01–50 in Kohn, 2008, which is located less than 1 km structurally below the MCT).

All of the other samples from the Gosainkund–Helambu section are two-mica/biotite schists or gneisses that do not show evidence of anatexis at the outcrop scale. They consist of chemically homogeneous minerals and do not preserve relicts of their prograde history. The estimated peak metamorphic conditions (734 ± 19 °C, 10 ± 0.8 kbar) lie in the kyanite stability field (Fig. 12b; Table 3). These peak temperatures are compatible with the beginning of partial melting, in agreement with microstructural observations (i.e. peritectic garnet, nanogranites) which suggest that these metapelites experienced an incipient partial melting, at temperatures below the white mica dehydration melting curve. The structurally highest sample does not show microstructural evidences of partial melting, probably due to the low amounts of white mica originally present in the rock. The estimated peak *P–T* conditions correspond to a *T/*depth ratio of 23 ± 3 °C km^{-1} (Table 3). The retrograde path for all these samples is characterized by cooling and decompression, still inside the kyanite stability field or in the sillimanite stability field.

Prior to our investigation, a limited number of *P–T* data on the Gosainkund–Helambu section were published. Apart from a couple of samples from the Gosainkund area investigated by Macfarlane (1995) and Fraser *et al*. (2000), giving *P–T* constraints of 640–680°C, 7.8–8.2 kbar, the only comprehensive study of this area is that by Rai *et al*. (1998). These authors applied both conventional and multi-equilibrium thermobarometry on nine metapelite samples. Although their data are affected by large uncertainties (especially on pressures), they are consistent with our results in showing a great homogeneity in peak *P–T* conditions along the transect, with *P-T* broadly in the range 670–700°C, 7.2–8.2 kbar (Rai *et al*., 1998).

Field data integrated with petrological results, help to correlate the samples from the Gosainkund–Helambu transect to those of the Langtang section, and allow the reconstruction of the tectono-metamorphic architecture of the GHS in the Gosainkund–Helambu region. The following observations can be made:

(i) Peak-*P* conditions recorded by the Gosainkund–Helambu samples are broadly homogeneous; no abrupt decreases in peak–*P* are observed along the transect, thus suggesting that the studied samples all belong to a coherent tectono-metamorphic unit;

(ii) the *T/*depth ratios recorded by the Gosainkund–Helambu metapelites is uniform (23 ± 3 °C km^{-1}) and consistent with that recorded by the L–GHS samples from the Langtang section (22 ± 1 °C km^{-1}) (Fig. 13; Table 3).

Overall, these observations suggest that the rocks in the Gosainkund–Helambu region belong entirely to the L-GHS unit. The Langtang Thrust (LT) which divides the GHS into two tectono-metamorphic units is structurally too high to be intersected in the Gosainkund–Helambu section.

Tectono-metamorphic architecture of the Gosainkund–Helambu area and implications for the Himalayan kinematic models

Our results have interesting implications for the interpretation of the Kathmandu Nappe (KN). The structural and metamorphic architecture of the KN has been recently reviewed by He *et al*. (2015) (refer to that paper and references therein for further details). Here we summarize the main points relevant to this discussion. The KN is conventionally divided, from top to bottom, in the Phulchauki Group, Bhimpedi Group and Sheopuri Gneiss. The Phulchauki Group is generally correlated to the TSS, whereas the interpretation of the Bhimpedi Group is debated. The Bhimpedi–Phulchauki succession is characterized by a right–way–up thermal gradient (Fig. 14a), ranging from the kyanite zone (~ 650°C) at its base to anchi-metamorphic or un-metamorphosed rocks at its top (Johnson *et al*., 2001; Webb *et al*., 2011). The Bhimpedi–Phulchauki succession occurs in the hanging wall of the Galchi Shear Zone (Webb *et al*., 2011), which separates the Bhimpedi and Phulchauki Groups from the Sheopuri Gneiss in the footwall. The Sheopuri Gneiss, thrust over the LHS by the MCT, is interpreted as belonging to the GHS. However, the correlation of the Sheopuri Gneiss to the Lower GHS vs. Upper GHS remained ambiguous so far.

Four structural models have been proposed to explain the architecture of the KN (He *et al*., 2015 and references therein) (Fig. 14a): Model A (Rai *et al*., 1998; Upreti & Le Fort, 1999; Hodges, 2000) considers the KN as entirely belonging to the LHS. This model has been recently criticized (e.g. He *et al*., 2015; Khanal *et al*., 2015). According to model B (Johnson *et al*., 2001; Gehrels *et al*., 2003; Robinson *et al*., 2003), the KN is completely ascribed to the GHS (i.e. the STDS does not occur in the KN). Model C (Khanal *et al*., 2015; see also Yin, 2006, although less explicit) correlates the KN to both the GHS (lower Bhimpedi Group) and the TSS (upper Bhimpedi Group + Phulchauki Group), thus implying that: (i) the STDS is located within the KN, separating the lower Bhimpedi Group from the upper Bhimpedi Group, and (ii) that the Galchi Shear Zone is an intra–GHS thrust juxtaposing two different GHS units. Khanal *et al*. (2015) further suggest that the Galchi Shear Zone correlates with the Langtang Thrust, which merges with the MCT on the northern side of the KN. According to this model, the lower Bhimpedi Group and the Sheopuri Gneiss can be thus correlated to the U–GHS and L–GHS, respectively. Model D (Webb *et al*., 2011; see also He *et al*., 2015) correlates the KN to the TSS. This model implies that the Galchi Shear Zone coincides with the STDS, which merges with the MCT on the northern side of the KN. According to this model the Bhimpedi Group and the Sheopuri Gneiss can be thus correlated to the TSS and L–GHS, respectively.

Our results demonstrate that the Sheopuri Gneiss should be correlated to the lower portion of the GHS (i.e. L–GHS), being the Gosainkund–Helambu region entirely carved within the L–GHS (i.e. all the studied samples along the Gosainkund–Helambu section experienced the same *P–T* evolution and are characterized by the same *T*/depth gradients as the L–GHS samples from the Langtang section). In considering on these results, the following issues arise: (i) If we interpret the Sheopuri Gneiss as the southern equivalent of the L–GHS, model B has serious geometrical problems to explain the right–way–up thermal gradient observed in the KN, opposite to the inverted thermal gradient observed northward within the GHS. In other words, there are no simple geometrical

features able to explain why the L–GHS is overlain by higher-grade rocks to the north and by lower-grade rocks to the south. (ii) Both models C and D are compatible with the correlation of the Sheopuri Gneiss to the L-GHS and are able to explain the right–way–up thermal gradient in the Bhimpedi–Phulchauki succession. He *et al*. (2015) and Khanal *et al*. (2015) also provided geochronological constraints on the movement of the Galchi Shear Zone. Although their results are very similar (i.e. 23.1–18.8 Ma: He *et al*., 2015; > 22.5 ± 2.3 Ma: Khanal *et al*., 2015), their final interpretations are significantly different. Being limited to the footwall of the Galchi Shear Zone, our results are not sufficient to definitively discriminate between models C and D. Conventional thermobarometric data published by Johnson *et al*. (2001) suggest that the base of the Bhimpedi Group experienced peak T ≤ 650°C (see also He *et al*., 2015 for similar temperatures obtained using the quartz c–axis thermometry method); these temperatures are significantly lower than those estimated for the U–GHS rocks in the Langtang region, and are not compatible with the widespread evidence of anatexis that characterize the U–GHS (sample 14–08a in this study). We therefore suggest that our results (i.e. Sheopuri Gneiss = L–GHS; > 770°C estimated for the U–GHS vs. ≤ 650°C reported for the Bhimpedi Group) better support model D rather than model C (Fig. 14a).

If we assume that the KN is correlated to the TSS (model D), further implications for the Himalayan kinematic models can be briefly discussed (for a more detailed and comprehensive discussion about the complexities of both the end-members and hybrid kinematic models see for example the reviews by Cottle *et al*., 2015 and He *et al*., 2015).

Among the end-member kinematic models commonly used to explain the evolution of the Himalaya, the critical taper (e.g. Hodges *et al*., 1992, 2001; Vannay & Grasemann, 2001; Kohn, 2008) and the wedge extrusion/channel flow (e.g. Burchfiel & Royden, 1985; Burchfiel *et al*., 1992; Grujic *et al*., 1996; Beaumont *et al*., 2001, 2004; Godin *et al*., 2006) models all imply that the TSS overlies the high-grade, migmatitic, upper portion of the GHS (U–GHS) (Fig. 14b). This is not consistent with our results, which demonstrate that the KN (equivalent to the TSS) directly overlies the L–GHS, not the U–GHS. Predictions of the tectonic wedge model (e.g. Webb *et al*., 2007) on the relative geometry of the TSS with respect to the L–GHS are more ambiguous (Fig. 14b). The only end-member model able to unambiguously predict the overlap of the TSS on the medium- to high-grade L–GHS is the duplexing model (e.g. Webb *et al*., 2013; Larson & Cottle, 2014; Cottle *et al*., 2015; Larson *et al*., 2015) (Fig. 14b). We therefore speculate that in this sector of the Himalayan chain, the most appropriate kinematic model able to explain the observed tectono-metamorphic architecture of the GHS is the duplexing model or hybrid models which combine the duplexing model with another end-member model (e.g. duplexing + tectonic wedge model: Webb *et al.,* 2013; He *et al*., 2015; duplexing + spatially and temporally evolving channel tunnelling/tectonic wedging model: Larson & Cottle, 2014; Cottle *et al*., 2015; Larson *et al*., 2015). This does not necessarily imply that the other kinematic models proposed were not relevant in different sectors of the Himalayan chain. As a provocative clue we notice that the L–GHS rocks in the studied area as well as in other sectors of western Nepal Himalaya (e.g. Carosi *et al*., 2010; Montomoli *et al*., 2013; Iaccarino *et al*., 2015) experienced clockwise *P–T* paths characterized by an increase in both pressure and temperature (i.e. peak-*P* is reached at peak–*T*). This *P–T* evolution is significantly different from that experienced by L–GHS rocks in the central-eastern Nepal Himalaya (e.g. Goscombe & Hand, 2000; Goscombe *et al*., 2006; Groppo *et al*., 2009; Mosca *et al*., Larson *et al*., 2013, 2012; Rolfo *et al*. 2015), where the clockwise *P–T* paths are characterized by heating during decompression (i.e. peak–*P* is reached prior

to peak–*T*). This could suggest different burial and exhumation mechanisms active in different sectors of the Himalayan chain (see also Cottle *et al*., 2015 for a discussion on this point).

ACKNOWLEDGEMENTS

Fieldwork and laboratory work was supported by the Ev–K2–CNR in collaboration with the Nepal Academy of Science and Technology, by the University of Torino–Call 1—Junior PI Grant (TO_Call1_2012_0068), by the Italian Ministry of University and Research (PRIN 2011–2010PMKZX7) and by Ricerca Locale (ex-60%—2014) funds of the University of Torino. Constructive reviews from A. Indares, K.P. Larson and an anonymous reviewer improved the final manuscript. The helpful suggestions and editorial handling by editor M. Brown were greatly appreciated.

REFERENCES

Ambrose, T.K., Larson, K.P., Guilmette, C., Cottle, J.M., Buckingham, H. & Rai, S., 2015. Lateral extrusion, underplating, and out-of-sequence thrusting within the Himalayan metamorphic core, Kanchenjunga, Nepal. *Lithosphere*, **7,** 441–464.

Arita, K., 1983. Origin of the inverted metamorphism of the Lower Himalayas Central Nepal: *Tectonophysics***, 95,** 43–60.

Beaumont, C., Jamieson, R.A., Nguyen, M.H. & Lee, B., 2001. Himalayan tectonics explained by extrusion of a low viscosity crustal channel coupled to focused surface denudation. *Nature*, **414,** 738–742.

Beaumont, C., Jamieson, R.A., Nguyen, M.H. & Medvedev, S., 2004. Crustal channel flows: 1. Numerical models with applications to the tectonics of the Himalayan-Tibetan orogeny. *Journal of Geophysical Research*, **109,** B06406.

Burchfiel, B.C. & Royden, L.H., 1985. North-south extension within the convergent Himalayan region. *Geology*, **13,** 679–682.

Burchfiel, B.C., Chen, Z., Hodges, K.V., Liu, Y., Royden, L.H., Deng, C. & Xu, J., 1992. The South Tibetan detachment system, Himalaya orogen: Extension contemporaneous with and parallel to shortening in a collisional mountain belt. *Geological Society of America Special Paper*, **269,** 41.

Carosi, R., Lombardo, B., Molli, G., Musumeci, G. & Pertusati, P.C., 1998. The South Tibetan Detachment System in the Rongbuk valley, Everest region. Deformation features and geological implications. *Journal of Asian Earth Sciences,* **16,** 299–311.

Carosi, R., Montomoli, C., Rubatto, D. & Visonà, D., 2010. Late oligocene high-temperature shear zones in the core of the Higher Himalayan Crystallines (Lower Dolpo, western Nepal). *Tectonics*, **29,** TC4029.

Cenki, B., Kriegsman, L.M. & Braun, I., 2002. Melt-producing and melt-consuming reactions in the Achankovil cordierite gneisses, South India. *Journal of Metamorphic Geology*, **20,** 543–561.

Cesare, B., Ferrero, S., Salvioli-Mariani, E., Pedron, D. & Cavallo, A., 2009. ''Nanogranite'' and glassy inclusions: the anatectic melt in migmatites and granulites. *Geology*, **37,** 627–630.

Clarke, G.L., White, R.W., Lui, S., Fitzherbert, J.A. & Pearson, N.J., 2007. Contrasting behaviour of rare earth and major elements during partial melting in granulite facies migmatites, Wuluma Hills, Arunta Block, central Australia. *Journal of Metamorphic Geology*, **25,** 1–18.

Corrie, S.L. & Kohn, M.J., 2011. Metamorphic history of the central Himalaya, Annapurna region, Nepal, and implications for tectonic models. *Geological Society of America Bulletin*, **123,** 1863–1879.

Cottle, J.M., Larson, K.P. & Kellett, D.A., 2015. How does the mid-crust accommodate deformation in large, hot collisional orogens? A review of recent research in the Himalayan orogen. *Journal of Structural Geology*, **78**, 119–133.

Fraser, G.,Worley, B. & Sandiford, M., 2000. High-precision geothermobarometry across the High Himalayan metamorphic sequence, Langtang Valley, Nepal. *Journal of Metamorphic Geology*, **18,** 665–681.

Gansser, A., 1964. Geology of the Himalaya. Wiley, Chichester.

Gehrels, G.E., DeCelles, P.G., Martin, A., Ojha, T.P., Pinhassi, G. & Upreti, B.N., 2003. Initiation of the Himalayan orogen as an early Paleozoic thin-skinned thrust belt. *GSA Today*, **13,** 4–9.

Godin, L., Grujic, D., Law, R. & Searle, M.P., 2006. Crustal flow, extrusion, and exhumation in continental collision zones: An introduction. In: Law, R., Searle, M.P. & Godin, L., eds. Channel flow, ductile extrusion, and exhumation in continental collision zones. *Geological Society, London, Special Publication*, **268,** 1–23.

Goscombe, B. & Hand, M., 2000. Contrasting P-T paths in the Eastern Himalaya, Nepal: Inverted isograds in a paired metamorphic mountain belt. *Journal of Petrology*, **41,** 1673–1719.

Goscombe, B., Gray, D. & Hand, M., 2006. Crustal architecture of the Himalayan metamorphic front in eastern Nepal. *Gondwana Research*, **10,** 232–255.

Groppo, C., Rolfo, F. & Indares, A., 2012. Partial melting in the Higher Himalayan Crystallines of Eastern Nepal: the effect of decompression and implications for the ''channel flow'' model. *Journal of Petrology*, **53,** 1057–1088.

Groppo, C., Rolfo, F. & Lombardo, B., 2009. P-T evolution across the Main Central Thrust Zone (Eastern Nepal): hidden discontinuities revealed by petrology. *Journal of Petrology*, **50,** 1149–1180.

Groppo, C., Rolfo, F. & Mosca, P., 2013. The cordierite-bearing anatectic rocks of the Higher Himalayan Crystallines (eastern Nepal): low-pressure anatexis, melt-productivity, melt loss and the preservation of cordierite. *Journal of metamorphic Geology,* **31,** 187–204.

Groppo, C., Rubatto, D., Rolfo, F. & Lombardo, B., 2010. Early Oligocene partial melting in the Main Central Thrust Zone (Arun Valley, eastern Nepal Himalaya). *Lithos,* **118,** 287–301.

Grujic, D., Casey, M., Davidson, C., Hollister, S. L., Kundig, R., Pavlis, T. & Schmid, S., 1996. Ductile extrusion of the Higher Himalayan Crystalline in Bhutan: evidence from quartz microfabrics. *Tectonophysics*, **260,** 21–43.

Hagen, T., 1969. Report on the geological survey of Nepal: Volume 1: Preliminary reconnaissance. *Zurich, Social Helvétique Sciences Natural Mémoir*, **86,** 185.

Harris, N.B.W. & Massey, J., 1994. Decompression and anatexis of Himalayan metapelites. *Tectonics*, **13,** 1537–1546.

He, D., Webb, A.A.G., Larson, K.P., Martin, A.J. & Schmitt, A.K., 2015. Extrusion vs. duplexing models of Himalayan mountain building. 3: Duplexing dominates from the Oligocene to Present. *International Geology Review*, **57,** 1–27.

Hodges, K.V., 2000. Tectonics of the Himalaya and southern Tibet from two perspectives. *Geological Society of America Bulletin*, **112,** 324–350.

Hodges, K.V., Hurtado, J.M. & Whipple, K.X., 2001. Southward extrusion of Tibetan crust and its effect on Himalayan tectonics. *Tectonics*, **20,** 799–809.

Hodges, K.V., Parrish, R.R., Housh, T.B., Lux, D.R., Burchfiel, B. C., Royden, L.H. & Chen, Z., 1992. Simultaneous Miocene extension and shortening in the Himalayan orogeny. *Science*, **258,** 1466–1470.

Holness, M.B. & Clemens, J. D., 1999. Partial melting of the Appin Quartzite driven by fracture controlled H_2O infiltration in the aureole of the Ballachulish Igneous Complex, Scottish Highlands. *Contributions to Mineralogy and Petrology*, **136,** 154–168.

Holness, M.B. & Sawyer, E.W., 2008. On the pseudomorphing of melt-filled pores during the crystallization of migmatites. *Journal of Petrology*, **49,** 1343–1363.

Iaccarino, S., Montomoli, C., Carosi, R., Massonne, H.J., Langone, A. & Visonà, D., 2015. Pressure-temperature-time-deformation path of kyanite-bearing migmatitic paragneiss in the Kali Gandaki valley (Central Nepal): Investigation of Late Eocene-Early Oligocene melting processes. *Lithos*, **231,** 103–121.

Imayama, T., Takeshita, T. & Arita, K., 2010. Metamorphic P–T profile and P–T path discontinuity across the far-eastern Nepal Himalaya: investigation of channel flow models. *Journal of Metamorphic Geology*, **28,** 527–549.

Imayama, T., Takeshita, T., Yi, K. *et al*., 2012. Two-stage partial melting and contrasting cooling history within the Higher Himalayan Crystalline Sequence in the far-eastern Nepal Himalaya. *Lithos*, **134-135**, 1–22.

Indares, A., White, R.W. & Powell, R., 2008. Phase equilibria modelling of kyanite-bearing anatectic paragneiss from the central Grenville Province. *Journal of Metamorphic Geology*, **26,** 815–836.

Inger, S. & Harris, N.B.W., 1992. Tectonothermal evolution of the High Himalayan Crystalline Sequence, Langtang Valley, northern Nepal. *Journal of Metamorphic Geology*, **10,** 439–452.

Jamieson, R.A., Beaumont, C., Medvedev, S. & Nguyen, M. H., 2004. Crustal channel flows: 2. Numerical models with implications for metamorphism in the Himalayan-Tibetan orogeny. *Journal of Geophysical Research*, **109,** B6.

Johnson, M.R.W., Oliver, G.J.H., Parrish, R.R. & Johnson, S.P., 2001. Synthrusting metamorphism, cooling, and erosion of the Himalayan Kathmandu complex, Nepal. *Tectonics*, **20,** 394–415.

Khanal, S., Robinson, D.M., Kohn, M.J. & Mandal, S., 2015. Evidence for a far-traveled thrust sheet in the Greater Himalayan thrust system, and an alternative model to building the Himalaya. *Tectonics*, **34**, 31–52.

Kellett, D.A., Grujic, D., Warren, C., Cottle, J., Jamieson, R. & Tenzin, T., 2010. Metamorphic history of a syn-convergent orogen-parallel detachment: the south Tibetan detachment system, eastern Himalaya. *Journal of metamorphic Geology*, **28,** 785–808.

Kohn M.J., 2004. Oscillatory- and sector-zoned garnets record cyclic (?) rapid thrusting in central Nepal. *Geochemistry Geophysics Geosysems*, **5,** Q12014.

Kohn M.J., 2014. Himalayan metamorphism and its tectonic implications. *Annual Reviews Earth Planetary Science*, **42,** 381–419.

Kohn, M.J., 2008. PTt data from central Nepal support critical taper and repudiate large-scale channel flow of the Greater Himalayan Sequence. *Geological Society of America Bulletin*, **120,** 259–273.

Kohn, M.J., Wieland, M.S., Parkinson, C.D. & Upreti, B.N., 2004. Miocene faulting at plate tectonic velocity in the Himalaya of central Nepal. *Earth and Planetary Science Letters*, **228,** 299–310.

Kohn, M.J., Wielnand, M., Parkinson, C. D. & Upreti, B.N., 2005. Five generation of monazite in Langtang gneisses: implication for chronology of the Himalayan metamorphic core. *Journal of Metamorphic Geology*, **23,** 399–406.

Kriegsman, L.M. & lvarez-Valero, A.M., 2010. Melt-producing versus melt-consuming reactions in pelitic xenoliths and migmatites. *Lithos*, **116,** 310–320.

Larson, K.P. & Cottle, J.M., 2014. Midcrustal discontinuities and the assembly of the Himalayan mid-crust. *Tectonics*, **33,** 718–740.

Larson, K.P., Gervais, F. & Kellett, D.A., 2013. A P–T–t–D discontinuity in east-central Nepal: Implications for the evolution of the Himalayan mid-crust. *Lithos* , **179**, 275–292.

Larson, K.P., Ambrose, T.K., Webb, A.G., Cottle, J.M. & Shrestha, S., 2015. Reconciling Himalayan midcrustal discontinuities: The Main Central thrust system. *Earth and Planetary Science Letters*, **429**, 139–146.

Larson, K.P., Godin, L. & Price, R.A., 2010. Relationships between displacement and distortion in orogens: Linking the Himalayan foreland and hinterland in central Nepal. *Geological Society of America Bulletin*, **122,** 1116–1134.

Le Fort, P., 1975. Himalaya: the collided range. Present knowledge of the continental arc. *American Journal of Science*, **275A,** 1–44.

Lombardo, B., Pertusati, P. & Borghi, A., 1993. Geology and tectono-magmatic evolution of the eastern OHimalaya along the Chomolungma–Makalu transect. In: Treloar, P. J. & Searle, M. P. (eds) Himalayan Tectonics. *Geological Society of London Special Publication ,* **74,** 341–355.

Macfarlane, A.M., 1993. Chronology of tectonic events in the crystalline core of the Himalaya, Langtang National Park, central Nepal. *Tectonics*, **12,** 1004–1025.

Macfarlane, A.M., 1995. An evaluation of the inverted metamorphic gradient at Langtang National Park, Central Nepal, Himalaya. *Journal of Metamorphic Geology*, **13,** 595–612.

Macfarlane, A.M., Hodges, K.V. & Lux, D., 1992. A structural analysis of the Main Central Thrust zone, Langtang National Park, central Nepal Himalaya. *Geological Society of America Bulletin*, **104,** 1389–1402.

Montomoli, C., Iaccarino, S., Carosi, R., Langone, A. & Visonà, D., 2013. Tectonometamorphic discontinuities within the Greater Himalayan Sequence in Western Nepal (Central Himalaya): Insights on the exhumation of crystalline rocks. *Tectonophysics,* **608,** 1349–1370.

Montomoli, C., Carosi, R. & Iaccarino, S., 2015. Tectonometamorphic discontinuities in the Greater Himalayan Sequence: a local or a regional feature? *Geological Society London Special Publications*, **412,** 25–41.

Mosca, P., Groppo, C. & Rolfo, F., 2012. Structural and metamorphic features of the Main Central Thrust Zone and its contiguous domains in the eastern Nepalese Himalaya. *Journal of Virtual Explorer, Electronic Edition*, **41,** paper 2.

Pearson, O.N. & DeCelles, P.G., 2005. Structural geology and regional tectonic significance of the Ramgarh Thrust, Himalayan fold-thrust belt of Nepal. *Tectonics*, **24,** TC4008.

Pêcher, A., 1989. The metamorphism in Central Himalaya. *Journal of Metamorphic Geology*, **7,** 31–41.

Pognante, U. & Benna, P., 1993. Metamorphic zonation, migmatization, and leucogranites along the Everest transect (eastern Nepal and Tibet): record of an exhumation history. In: Treloar, P.J. & Searle, M. P. (eds), Himalayan Tectonics. *Geological Society of London, Special Publication*, **74,** 323-340.

Rai, S.M., Guillot, S., Le Fort, P. & Upreti, B.N., 1998. Pressure-temperature evolution in the Kathmandu and Gosainkund regions, Central Nepal. *Journal of Asian Earth Sciences*, **16,** 283–298.

Reddy, S.M., Searle, M.P. & Massey, J.A., 1993. Structural evolution of the High Himalayan gneiss sequence, Langtang Valley, Nepal. In: Treloar, P.J. & Searle, M.P., (eds), Himalayan Tectonics. *Geological Society of London, Special Publication,* **74,** 375–389.

Robinson, D.M., DeCelles, P.G., Garzione, C.N., Pearson, O.N., Harrison, T.M. & Catlos, E.J., 2003. Kinematic model for the Main Central Thrust in Nepal. *Geology*, **31,** 359–362.

Rolfo, F., Groppo, C. & Mosca, P., 2015. Petrological constraints of the "Channel Flow" model in eastern Nepal. In: Mukherjee, S., Carosi, R., van der Beek, P.A., Mukherjee, B.K. & Robinson, D.M. (eds), Tectonics of the Himalaya. *Geological Society London Special Publications*, **412,** 177–197.

Searle, M.P., Law, R.D., Godin, L., Larson, K.P., Streule, M.J., Cottle, J.M. & Jessup, M.J., 2008. Defining the Himalayan Main Central Thrust in Nepal. *Journal of Geological Society of London* , **165,** 523–534.

Stöcklin, J., 1980. Geology of Nepal and its regional frame: Thirty-third William Smith lecture. *Journal of the Geological Society*, **137,** 1–34.

Takagi, H., Arita, K., Sawaguchi, T., Kobayashi, K. & Awaji, D., 2003. Kinematic history of the Main Central Thrust zone in the Langtang area, Nepal. *Tectonophysics*, **366**, 151– 163.

Upreti, B.N. & Le Fort, P., 1999. Lesser Himalayan crystalline nappes of Nepal: Problem of their origin. In Macfarlane, A., Quade, J. & Sorkhabi, R., (eds), Himalaya and Tibet: Mountain roots to mountain tops. *Geological Society of America Special Paper,* **328,** 225–238.

Upreti, B.N., 1999. An overview of the stratigraphy and tectonics of the Nepal Himalaya. *Journal of Asian Earth Sciences*, **17,** 577–606.

Vannay, J.C. & Grasemann, B., 2001. Himalayan inverted metamorphism and syn-convergence extension as a consequence of a general shear extrusion. *Geological Magazine*, **138,** 253–276.

Visonà, D. & Lombardo, B., 2002. Two mica- and tourmaline leucogranites from the Everest–Makalu region (Nepal-Tibet): Himalayan leucogranite genesis by isobaric heating? *Lithos*, **62,** 125-150.

Wang, J-M., Zhang, J-J., Liu, K., Wang, X-X., Rai, S., Scheltens, M., 2016. Spatial and temporal evolution of tectonometamorphic discontinuities in the Central Himalaya: Constraints from P-T paths and geochronology. *Tectonophysics,* **679**, 41-60.

Waters, D.J., 2001. The significance of prograde and retrograde quartz-bearing intergrowth microstructures in partially melted granulite-facies rocks. *Lithos,* **56,** 97–110.

Webb, A.A.G., Schmitt, A.K., He, D. & Weigand, E.L., 2011. Structural and geochronological evidence for the leading edge of the Greater Himalayan Crystalline complex in the central Nepal Himalaya. *Earth and Planetary Science Letters*, **304,** 483–495.

Webb, A.A.G., Yin, A. & Dubey, C.S., 2013. U-Pb zircon geochronology of major lithologic units in the eastern Himalaya: Implications for the origin and assembly of Himalayan rocks. *Geological Society of America Bulletin*, **125,** 499–522.

Webb, A.A.G., Yin, A., Harrison, T.M., Célérier, J. & Burgess, W.P., 2007. The leading edge of the Greater Himalayan Crystalline complex revealed in the NW Indian Himalaya: Implications for the evolution of the Himalayan Orogen. *Geology*, **35,** 955–958.

White, R.W., Powell, R. & Holland, T.J.B., 2001. Calculation of partial melting equilibria in the system Na_2O-CaO-K_2O-FeO-MgO-Al_2O_3-SiO_2-H_2O (NCKFMASH). *Journal of Metamorphic Geology* , **19,** 139–153.

Whitney, D.L., & Evans, B.W., 2010. Abbreviations for names of rock-forming minerals. *American Mineralogist*, **95,** 185–187.

Yakymchuk, C. & Godin, L., 2012. Coupled role of deformation and metamorphism in the construction of inverted metamorphic sequences: An example from far-northwest Nepal. *Journal of Metamorphic Geology*, **30,** 513–535.

Yin, A., 2006. Cenozoic tectonic evolution of the Himalayan orogen as constrained by along-strike variation of structural geometry, exhumation history, and foreland sedimentation. *Earth-Science Reviews*, **76,** 1–131.

SUPPORTING INFORMATIONS

Additional Supporting Information may be found in the online version of this article at the publisher's web-site:

Appendix S1 Methods: mineral chemistry, micro-X-ray fluorescence (μ-XRF) maps of the thin sections, estimate of the bulk compositions, pseudosection modelling.

Figure S1. Additional representative images (BSE) of nanogranites included in garnet from the L–GHS two-mica schists.

Figure S2. Crystallization–deformation relations of the studied samples, with mineral compositions and a synthesis of the thermobarometric results.

Figures S3–S6. *P–T* pseudosections modelled for the samples from the Langtang section: 14–03 (Fig. S3), 14–25b (Fig. S4), 14–24 (Fig. S5) and 14–08a (Fig. S6).

Tables S1–S3. Representative SEM–EDS analyses of minerals.

Table S4. Summary of the peak *P–T* constraints (with errors) and T/depth ratios for the Kohn (2008) samples.

Received 21 April 2016; revision accepted 16 August 2016.

Figure captions

Fig. 1. (a) Geological sketch map of the central–eastern Nepal Himalaya, showing major tectono-metamorphic units (modified from Goscombe & Hand, 2000, He *et al.*, 2015, Wang *et al*., 2016 and based on our own data). The white rectangle indicates the study area, reported in Fig. 1b. 1: Siwalik deposits; 2: Lesser Himalayan Sequence; 3: Lower Greater Himalayan Sequence; 4: Upper Greater Himalayan Sequence; 5: Tethyan Sedimentary Sequence. MFT: Main Frontal Thrust; MBT: Main Boundary Thrust; MCT: Main Central Thrust; STDS: South Tibetan Detachment System. The inset locates the study area in the framework of the Himalayan chain. **(b)** Geological map and representative cross sections of the Langtang and Gosainkund–Helambu regions (central Nepal Himalaya). GSZ: Galchi Shear Zone (from He *et al*., 2015); MCT: Main Central Thrust; LT: Langtang Thrust.

Fig. 2. Micro-XRF maps of the modelled metapelites from the Gosainkund–Helambu and Langtang sections. Sample 14–27a is not reported because its grain-size is too fine to allow a precise interpretation of the mineral distribution and to estimate the modal amount of each phase. Samples are reported from lower to upper structural level in both the sections.

Fig. 3. Representative microstructures of the metapelite samples from the Gosainkund–Helambu section. **(a, b)** Sample 14–27a. (a) Garnet porphyroblasts are wrapped around by the main foliation defined by the alignment of biotite + white mica + graphite. Note the rotated internal schistosity in garnet (Plane Polarized Light: PPL). (b) Detail of a microlithon, preserving an older foliation S_{m-1}

defined by white mica + biotite + chlorite + ilmenite ± plagioclase. Note the static growth of a large biotite flake on S_m, and chlorite replacing it at its rims (Back Scattered Electron image: BSE). **(c, d)** Sample 14–44a. (c) The schistosity is defined by the alignment of biotite + white mica; garnet porphyroblasts are in equilibrium with S_m (PPL). (d) Detail of a garnet porphyroblast shown in (c), its rim being in equilibrium with kyanite (PPL). The black arrow indicates a garnet zone rich in nanogranites. **(e, f)** Sample14–61b. (e) The main foliation, marked by the alignment of biotite + white mica, wraps around a garnet porphyroblast with numerous rounded inclusions (PPL). (f) Detail of a peritectic garnet growing around rounded inclusions of white mica + plagioclase + quartz + ilmenite (Crossed Polarized Light: XPL). **(g)** Sample 14–71. Garnet porphyroblasts are partially wrapped by the S_m, but the rims show equilibrium contacts with biotite + white mica defining the S_m (PPL). **(h, i)** Sample 14–52. (h) Detail of a garnet porphyroblast wrapped by the main foliation, defined by the alignment of biotite + sillimanite. The inset shows a relict kyanite replaced by plagioclase (PPL). (i) Detail of the banded structure characterized by cm-thick mesocratic layers consisting of biotite + sillimanite + quartz + plagioclase and mm-thick leucocratic quartz + sillimanite + plagioclase domains (PPL).

Fig. 4. Representative microstructures of the metapelite samples from the Langtang section**. (a, b)** Sample 14–03. (a) The main foliation is defined by the alignment of muscovite and biotite; garnet porphyroblasts are in equilibrium contact with both the sheet silicates (PPL). (b) Detail of a garnet porphyroblast; garnet core includes coarse-grained rounded quartz, ilmenite and rutile, whereas garnet rim is almost free of inclusions. The transition from core to rim is underlined by the presence of nanogranites (black arrow). The inset shows a detail of a nanogranite (BSE). **(c, d)** Sample 14–25b. (c) The main foliation is marked by the alignment of white mica and biotite; garnet rim shows equilibrium relationship with mica. Note the kyanite porphyroblasts, either aligned parallel to the main foliation or overgrowing it (PPL). (d) Detail of a staurolite porphyroblast including kyanite (PPL). **(e–g)** Sample 14–24. (e) The gneissic fabric is defined by micaceous layers alternating to quartz–rich domains. The main foliation is defined by the alignment of white mica, biotite and kyanite (PPL). (f) Detail of a garnet porphyroblast shown in (e), whose rim is in equilibrium with kyanite. The transition from core to rim is underlined by the presence of nanogranites (black arrow) (PPL). The inset shows a detail of a nanogranite (BSE). (g) Detail of a kyanite crystal rimmed by staurolite (BSE). **(h, i)** Sample 14–08a. (h) The gneissic fabric is defined by biotite + sillimanite ± garnet domains alternating with quartz feldspathic leucocratic layers. The inset shows a detail of garnet with location of nanogranites (white arrows). (h) Detail of a pseudomorph after melt (Holness & Clemens, 1999; Holness & Sawyer, 2008), defined by a thin film of quartz with a cuspate shape (XPL). The inset shows a biotite + sillimanite + quartz symplectite replacing rounded K-feldspar (BSE).

Fig. 5. Compositional diagrams for biotite (a, e), garnet (c, g), white mica (b, f) and plagioclase (d, h) in the studied samples from the Gosainkund–Helambu (a–d) and Langtang (e–h) transects, respectively. For each sample, biotite, muscovite and plagioclase have been distinguished according to their microstructural position (diamond: in equilibrium with S_{m-1}; circle: in equilibrium with S_m; square: post-S_m). Garnet zoning from core to rim is pointed out in (c) and (g) with coloured arrows.

Fig. 6. Zoning profiles of garnet from the Gosainkund–Helambu **(a)** and Langtang **(b)** sections, respectively. Relative distance between point analyses is not to scale. The diameter of the analysed garnet crystals is also reported. XCa, XMg, XFe and XMn defined as: XCa=Ca/(Mg+Fe+Ca+Mn);

XMg=Mg/(Mg+Fe+Ca+Mn); XFe=Fe/(Mg+Fe+Ca+Mn); XMn=Mn/(Mg+Fe+Ca+Mn).

Fig. 7. *P–T* pseudosection for sample 14–27a (Gosainkund-Helambu section) calculated in the MnNKCFMASTH system at $a(H_2O)=1$. **(a)** *P–T* pseudosection calculated using the whole–rock bulk composition, used to model the *P–T* conditions for the growth of garnet core. **(b)** Detail of (a) with compositional isopleths of garnet core. **(c)** *P–T* pseudosection calculated using the fractionated bulk composition, used to model the *P–T* conditions for the growth of garnet rim, contoured for garnet rim composition. In (a–c), white, light–, medium–, dark– and very dark– grey fields are di– tri–, quadri–, quini– and esa–variant fields, respectively. Ms and Pg refer to K–rich and Na–rich white mica, respectively. The white dashed rectangle in (a) refers to the *P–T* interval shown in (b), (c) and (d). The white dashed polygons in (b) and (c) constrain the *P–T* conditions of garnet core and rim growth, respectively. **(d)** *P–T* path inferred for sample 14–27a on the basis of mineral assemblages and compositions (light blue arrow). The dashed–line arrow represents the inferred retrograde *P–T* path.

Fig. 8. (a) *P–T* pseudosection for sample 14–44a (Gosainkund–Helambu section) calculated in the MnNKCFMASTH system at $a(H_2O)=1$. Variance of the fields as in Fig. 7. Ms and Pg refer to K–rich and Na–rich white mica, respectively. The white dashed rectangle refers to the *P–T* interval shown in (b) and (c). **(b)** Detail of (a) contoured for garnet composition. The white dashed polygon constrains the *P–T* conditions for the growth of the peak mineral assemblage. **(c)** *P–T* trajectory inferred for sample 14–44a on the basis of mineral assemblages and compositions (yellow arrow). The dotted–line (melt–in) in (a) to (c) represents the H_2O-saturated solidus.

Fig. 9. (a) *P–T* pseudosection for sample 14–61b (Gosainkund–Helambu section) calculated in the MnNKCFMASTH system. Variance of the fields as in Fig. 7. The white dashed rectangle refers to the *P–T* interval shown in (b) and (c). **(b)** Detail of (a) contoured for garnet composition. The white dashed polygon constrains the *P–T* conditions for the growth of peritectic garnet. **(c)** *P–T* path inferred for sample 14–61b (pink arrow). The dotted–line (melt–in) in (b) and (c) represents the solidus.

Fig. 10. (a) *P–T* pseudosection for sample 14–71 (Gosainkund–Helambu section) calculated in the MnNKCFMASTH system at $a(H_2O)=1$. Variance of the fields as in Fig. 7. Ms and Pg refer to K–rich and Na–rich white mica, respectively. The white dashed rectangle refers to the *P–T* interval shown in (b) and (c). **(b)** Detail of (a) contoured for garnet composition. The white dashed polygon constrains the *P–T* conditions for the growth of the peak mineral assemblage. **(c)** *P–T* path inferred for sample 14–71 (purple arrow); note that the occurrence of rare late sillimanite implies that the retrograde *P–T* trajectory enters the sillimanite stability field. The dotted–line (melt–in) in (a) to (c) represents the H_2O-saturated solidus.

Fig. 11. (a) *P–T* pseudosection for sample 14–52 (Gosainkund–Helambu section) calculated in the MnNKCFMASTH system at $a(H_2O)=1$. Variance of the fields as in Fig. 7. Ms and Pg refer to K–rich and Na–rich white mica, respectively. The white dashed rectangle refers to the *P–T* interval shown in (b) and (c). **(b)** Detail of (a) contoured for garnet composition. The white dashed polygon constrain the *P–T* conditions for the growth of garnet (peak *P–T* conditions). **(c)** *P–T* trajectory inferred for the

metapelite sample 14–52 (blue arrow). The dotted–line (melt–in) in (a) to (c) represents the H_2O-saturated solidus.

Fig. 12. *P–T* diagrams showing the *P–T* trajectories obtained for the modelled metapelites from the Langtang **(a)** and Gosainkund–Helambu **(b)** sections. The dotted and continuous dark grey lines represent the H_2O-saturated solidus and the white mica–out reaction, respectively (modified from White *et al*., 2001); these curves delimitate the white mica dehydration melting field (light grey) from the biotite dehydration melting field (dark grey).

Fig. 13. *T/*depth ratios (°C km^{-1}) (with errors) plotted as a function of the structural position for the samples studied in this paper (squares) and those studied by Kohn (2008) (diamonds) (his ZG1 to ZG4 zones). The dashed and dotted lines are the average *T/*depth values obtained from the studied samples and from those of Kohn (2008), respectively. It is evident that the L–GHS and U–GHS samples define two distinct clusters of *T/*depth ratios (orange and red boxes).

Fig. 14. (a) Structural models of the Kathmandu Nappe (modified from He *et al*., 2015). Reference papers for each models are: (A) Rai *et al*. (1998), Upreti & Le Fort (1999), Hodges (2000); (B) Johnson *et al*. (2001), Gehrels *et al*. (2003), Robinson *et al*. (2003); (C) Khanal *et al*. (2015); Yin (2006); (D) Webb *et al*. (2011). The colours from yellow to red imply increasing metamorphic grade in the GHS; the colours from light grey to dark grey imply increasing metamorphic grade in the TSS (see also the black arrows). Units in the Kathmandu Nappe are: BG: Bhimpedi Group; PG: Phulchauki Group; SG: Sheopuri Gneiss. LHS: Lesser Himalayan Sequence; L–GHS: Lower Greater Himalayan Sequence; U–GHS: Upper–Greater Himalayan Sequence; TSS: Tethyan Sedimentary Sequence. MCT: Main Central Thrust; LT: Langtang Thrust; STDS: South Tibetan Detachment System; GSZ: Galchi Shear Zone. **(b)** Sketch of the main current Himalayan tectonic models for the exhumation of GHS (modified from Montomoli *et al*., 2013, Cottle *et al*., 2015 and He *et al*., 2015). Colours and abbreviations as in (a) and in Fig. 1; ITS: Indus–Tsangpo suture.

Table 1. Bulk compositions of the modelled metapelites (mol%)

	14-27a	14-27a*	14-44a	14-61b	14-71	14-52	14-03	14-03*	14-25b	14-25b*	14-24	14-08a
SiO_2	67.45	67.47	68.05	69.36	75.57	71.01	71.27	71.86	63.81	65.24	70.7	73.94
TiO_2	0.62	0.62	0.53	0.52	0.6	0.95	0.69	0.70	0.61	0.62	0.61	0.50
Al_2O_3	16.42	16.39	16.24	10.81	11.63	8.91	13.82	13.81	17.77	18.02	14.01	10.71
FeO	6.60	6.52	4.75	6.23	5.49	7.25	6.10	5.60	7.68	5.89	6.12	3.97
MgO	1.96	1.96	3.18	2.16	1.74	6.63	2.85	2.76	3.05	2.91	2.59	1.47
MnO	0.15	0.13	0.12	0.10	0.12	0.07	0.20	0.16	0.24	0.07	0.21	0.09
CaO	0.88	0.86	0.84	0.64	0.32	0.61	0.45	0.40	0.56	0.49	3.28	1.02
Na_2O	0.80	0.80	1.76	3.41	1.00	1.83	0.72	0.73	1.77	1.90	0.72	2.02
K_2O	5.24	5.25	4.63	3.10	3.53	2.75	3.91	3.99	3.54	4.86	3.65	2.55
H_2O				3.68								3.73

The asterisk (*) refers to the fractionated bulk compositions (i.e. whole-rock composition minus garnet core composition) used to model the growth of garnet rim.

Table 2a. Mineral composition and modes for the metapelite samples from the Gosainkund–Helambu section

	Grt →	**Bt**	**Wm**	**Pl** →	**Kfs**	**Qz**	**Als**	**Chl**	**Ep**
14–27a	XMg=0.03–0.06 XCa=0.25–0.19 XMn=0.15–0.05 XFe=0.57–0.72	XMg=0.38–0.43 Ti=0.09–0.13	$Si^{\#}$=3.05–3.13 $Na^{\#}$=0.08–0.14 Si=3.05–3.17 Na=0.06–0.14	XAn=0.34–0.28				XMg^{i}=0.39 $XMg^{\#}$=0.41–0.44 XMg*=0.41–0.44	XZo=0.40–0.55
vol%	*1*	*12*	*53*	*3*		*26*		*5*	*<1*

14–44a	XMg=0.16–0.18 XCa=0.04–0.05 XMn=0.05–0.06 XFe=0.72–0.75	XMg^{i}=0.57–0.60 Ti^{i}=0.11–0.15 XMg=0.45–0.49 Ti=0.16–0.19	Si=3.16–3.07 Na=0.09–0.12 Si*=3.07–3.12 Na*=0.10	XAn=0.18–0.26			Ky
vol%	*4*	*11*	*45*	14		*24*	*2*
14–61b	XMg=0.12–0.13 XCa=0.02–0.03 XMn=0.03–0.04 XFe=0.80–0.84	XMg^{i}=0.26–0.29 Ti^{i}=0.11–0.16 XMg=0.28–0.34 Ti=0.11–0.21	Si^{i}=3.11–3.15 Na^{i}=0.05–0.06 Si=3.07–3.11 Na=0.05–0.09	XAn^{i}=0.11–0.12 XAn=0.02–0.10	XOr=0.87–0.93		
vol%	*5*	*15*	*15*	*30*	*7*	*28*	
14–71	XMg=0.10–0.11 XCa=0.04–0.03 XMn=0.04 XFe=0.84–0.87	XMg^{i}=0.35–0.42 Ti^{i}=0.22–0.23 XMg=0.28–0.36 Ti=0.15–0.25	Si=3.06–3.10 Na=0.12–0.14	XAn^{i}=0.18–0.20 XAn=0.14			Sil
vol%	*5*	*9*	*35*	*6*		*44*	*rare*
14–52	XMg=0.20–0.21 XCa=0.025–0.03 XMn=0.11–0.12 XFe=0.64–0.67	XMg^{i}=0.50 Ti^{i}=0.12 XMg=0.47–0.55 Ti=0.14–0.23	Si^{i}=3.08 Na^{i}=0.045	XAn=0.12–0.15			Ky^{r}/Sil
vol%	*1*	*36*	*<1*	*18*			*4*

^{i} included in garnet; $^{\#}$ defining S_{m-1}; * overgrowing S_m; ^{r} relict; The arrows indicate a zonation from core to rim; Ti, Si,Na are expressed as a.p.f.u.

Table 2b. Mineral composition and modes for the metapelite samples from the Langtang section

	Grt	Bt	Wm	Pl	St	Kfs	Qz	Als
	→			→				
	XMg=0.14–0.18	XMg^{i}=0.61–0.68	Si=3.09–3.14	XAn=0.17–0.22				Sil^{f}
14–03	XCa=0.075–0.05	Ti^{i}=0.09–0.12	Na=0.13–0.14					
	XMn=0.07–0.04	XMg=0.44–0.51						
	XFe=0.71–0.74	Ti=0.10–0.18						
vol%	*10*	*5*	*47*	*3*			*35*	*rare*
	→				→			
	XMg=0.13–0.15	XMg^{i}=0.44–0.54	Si=3.07–3.10	XAn^{i}=0.12	XMg=0.16–0.12			Ky/Sil^{f}
14–25b	XCa=0.04–0.03	Ti^{i}=0.10–0.14	Na=0.15–0.17	XAn=0.15–0.16				
	XMn=0.05–0.04	XMg=0.38–-0.46						
	XFe=0.78–0.81	Ti=0.10–0.17						
vol%	9	*11*	*48*	*10*	*1*		*18*	*3*
	→			→	→			
	XMg=0.14–0.16	XMg^{i}=0.50–0.55	Si=3.08–3.15	XAn^{i}=0.23	XMg=0.16–0.14			Ky
14–24	XCa=0.05–0.04	Ti^{i}=0.13–0.16	Na=0.13–0.14	XAn=0.15–0.22				
	XMn=0.05–0.04	XMg=0.41–0.47						
	XFe=0.75–0.79	Ti=0.10–0.24						
vol%	*9*	*8*	*39*	*10*	*<1*		*33*	*<1*
				→				
	XMg=0.10–0.12	XMg^{i}=0.37–0.38	Si*=3.07–3.10	XAn^{i}=0.33		XOr=0.90		Sil
14–08a	XCa=0.04–0.05	Ti^{i}=0.17	Na*=0.05–0.10	XAn=0.26–0.03				
	XMn=0.07–0.08	XMg=0.29–0.33						
	XFe=0.78–0.81	Ti=0.23–0.30						
vol%	*2*	*12*	*3*	*20*		*14*	*41*	*8*

^{i} included in garnet; * overgrowing S_m; ^{f} fibrolitic, replacing Grt and Wm at the rims; The arrows indicate a zonation from core to rim; Ti, Si,Na are expressed as a.p.f.u.

Table 3. Summary of the peak *P–T* constraints obtained from pseudosections (with errors) and *T*/depth ratios

		Sample	min *T* (°C)	max *T* (°C)	min *P* (kbar)	max *P* (kbar)	min depth (km)	max depth (km)	min *T*/depth (°C km^{-1})	max *T*/depth (°C km^{-1})	average *T* (°C)	error *T* (°C)	average *P* (kbar)	error *P* (kbar)	average *T*/depth (°C km^{-1})	error *T*/depth (°C km^{-1})
Langtang section	**U–GHS**	14-08	760	800	7	8.5	23	28	27	34	780	20	7.8	0.8	**31**	**4**
	L–GHS	14-24	725	760	9.7	10.8	32	36	20	24	743	18	10.3	0.6	22	2
		14-25b	715	725	9.7	10.0	32	33	21	22	720	5	9.9	0.2	22	0.5
		14-03	710	730	9.6	11.0	32	37	19	23	720	10	10.3	0.7	21	2
		L-GHS (average)	*717*	*738*	*10*	*10.6*	*32*	*35*	*20*	*23*	*728*	*11*	*10*	*0.5*	***22***	***1***
Gosainkund–Helambu section	**L–GHS**	14-52	720	760	9.0	10.0	30	33	22	25	740	20	9.5	0.5	23	2
		14-71	710	750	8.5	10.8	28	36	20	26	730	20	9.7	1.2	23	3
		14-61b	730	750	9.4	11.3	31	38	19	24	740	10	10.4	1.0	22	2
		14-44a	700	750	8.6	10.0	29	33	21	26	725	25	9.3	0.7	24	3
		L-GHS (average)	*715*	*753*	*9*	*10.5*	*30*	*35*	*20*	*25*	*734*	*19*	*10*	*0.8*	***23***	***3***
	LHS	14-27a	570	620	6.7	8.2	22	27	21	28	595	25	7.5	0.8	**24**	**3**

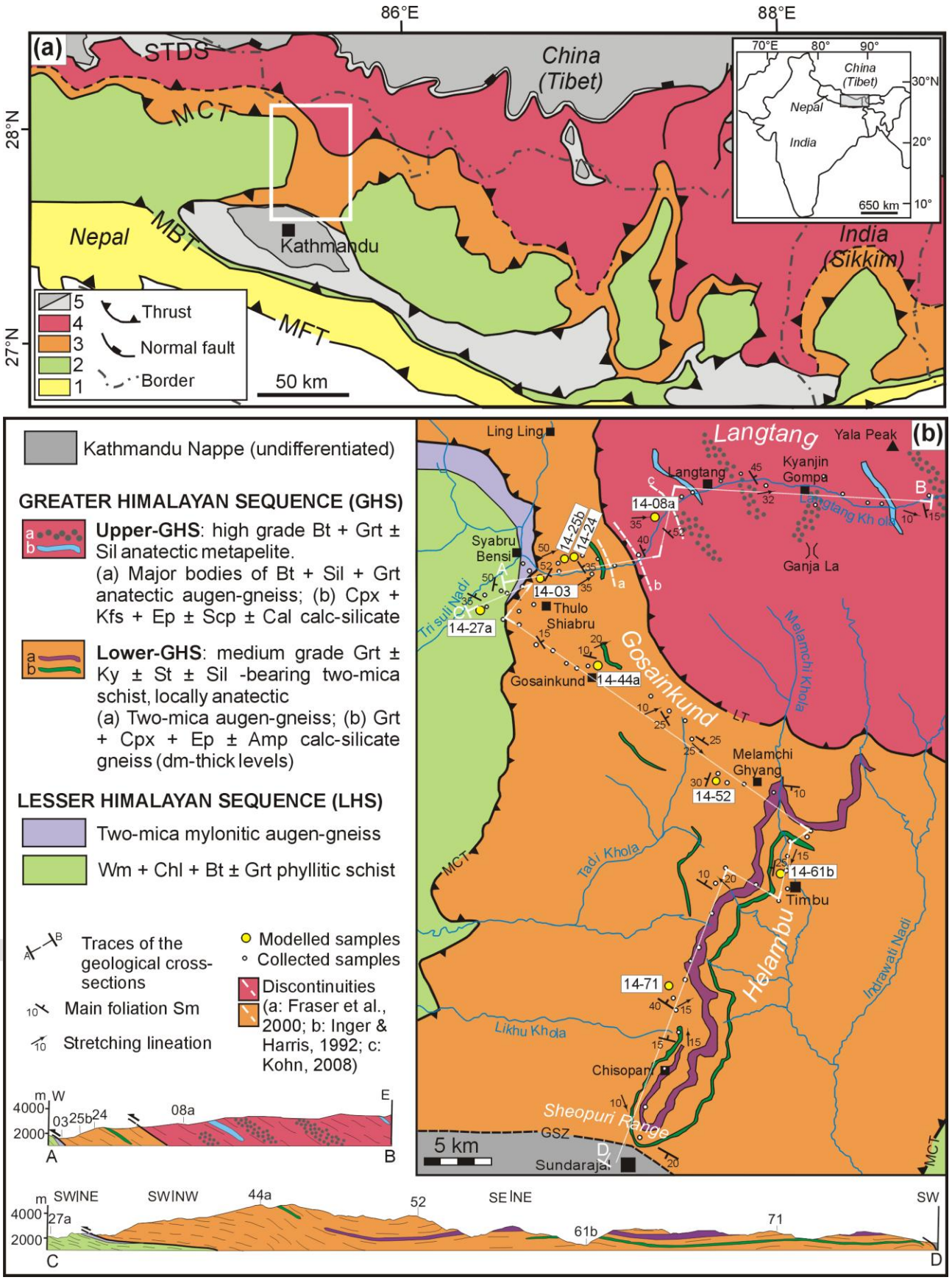

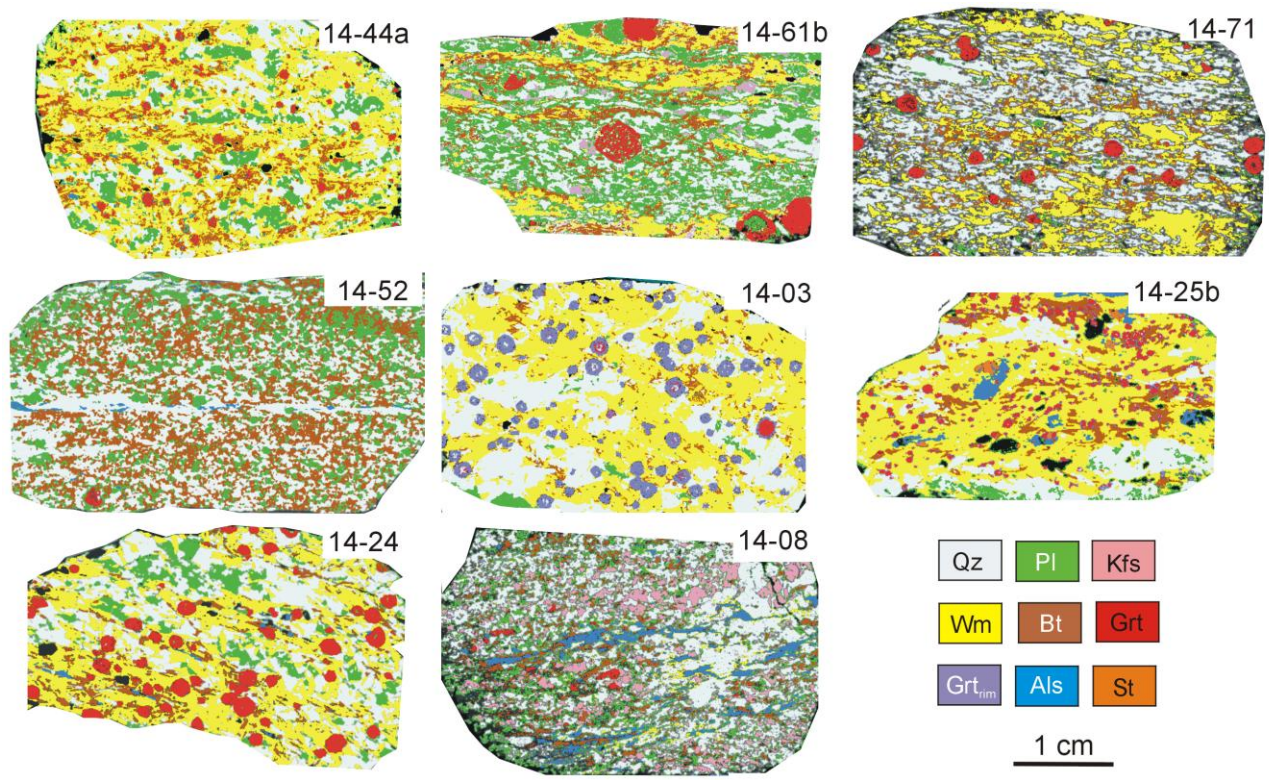

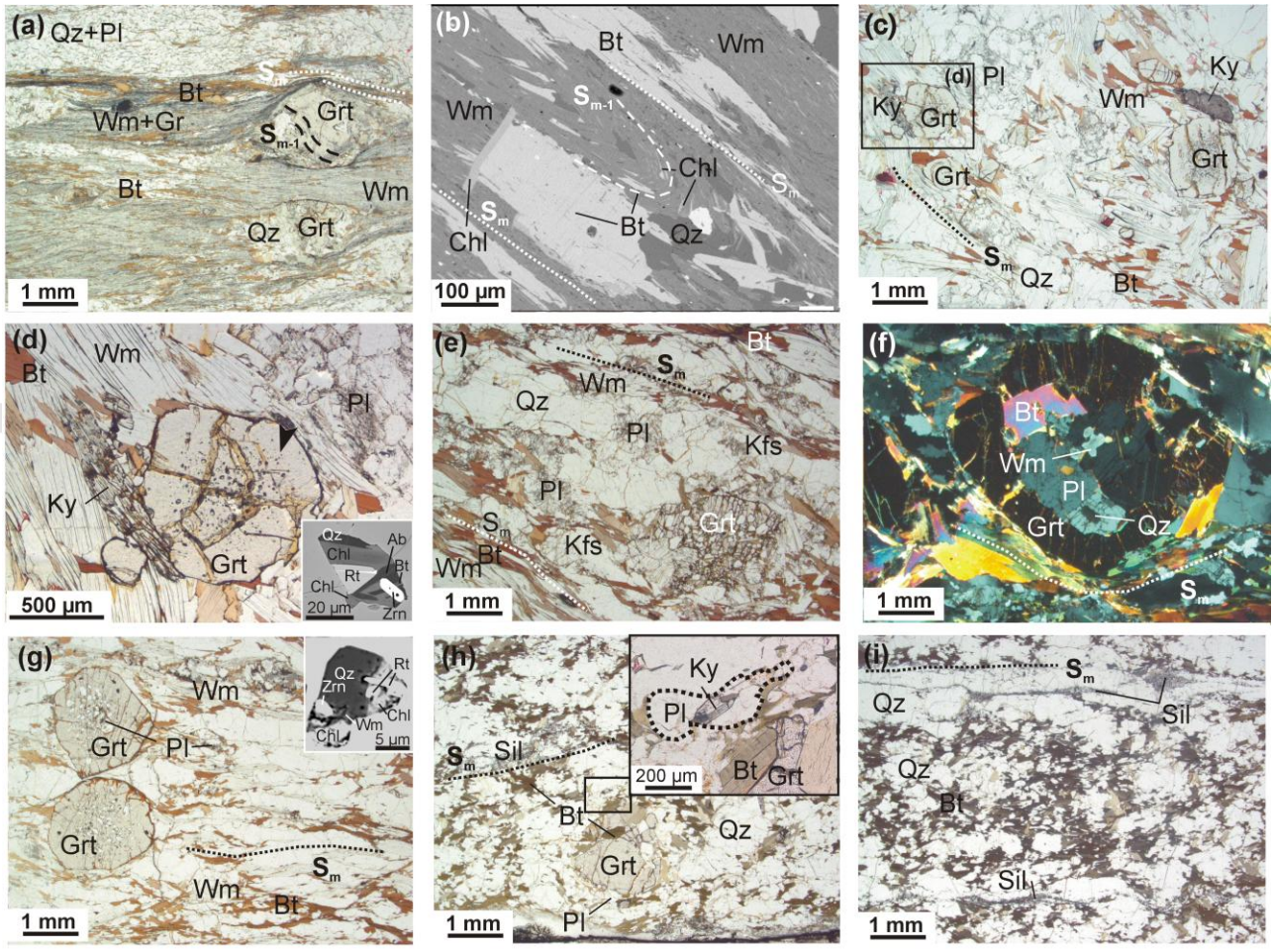

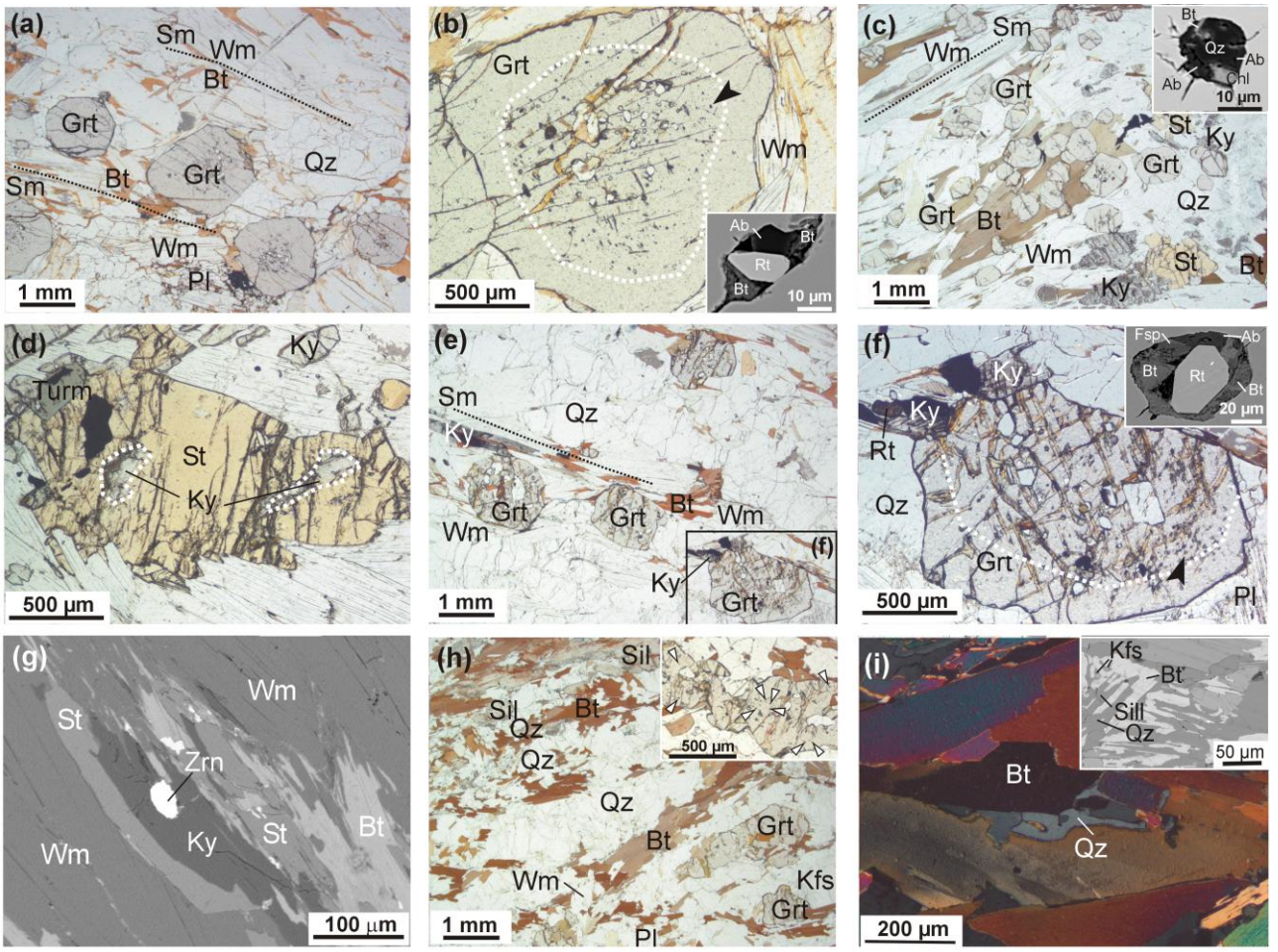

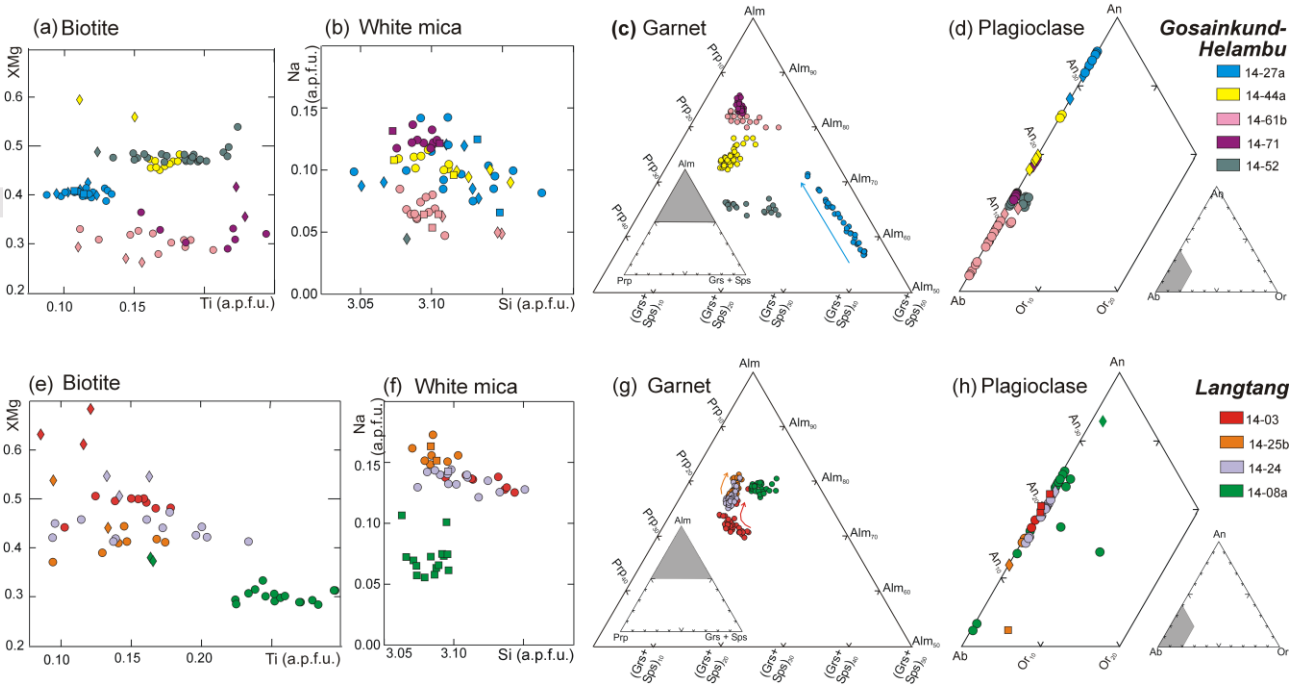

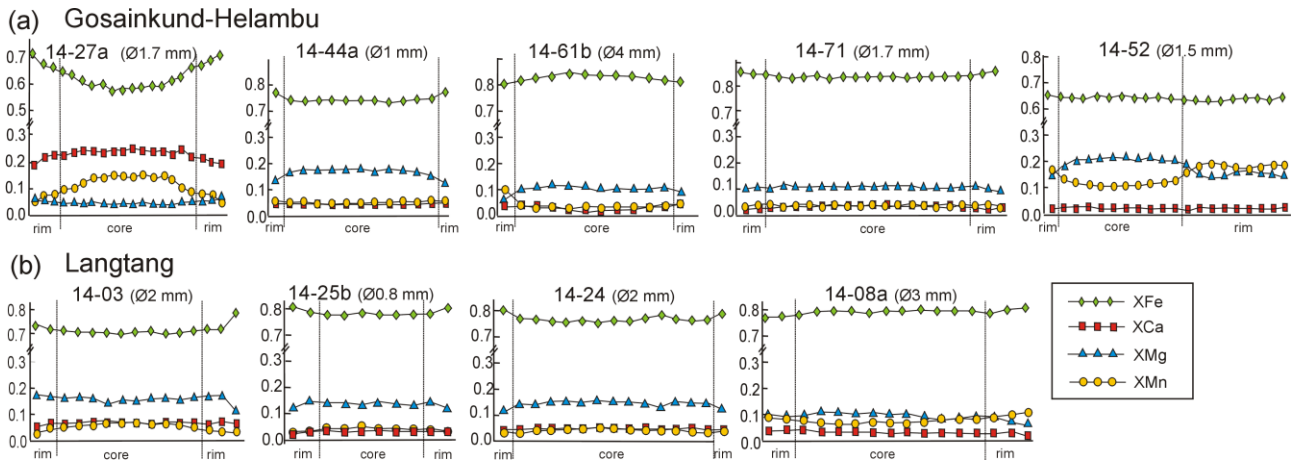

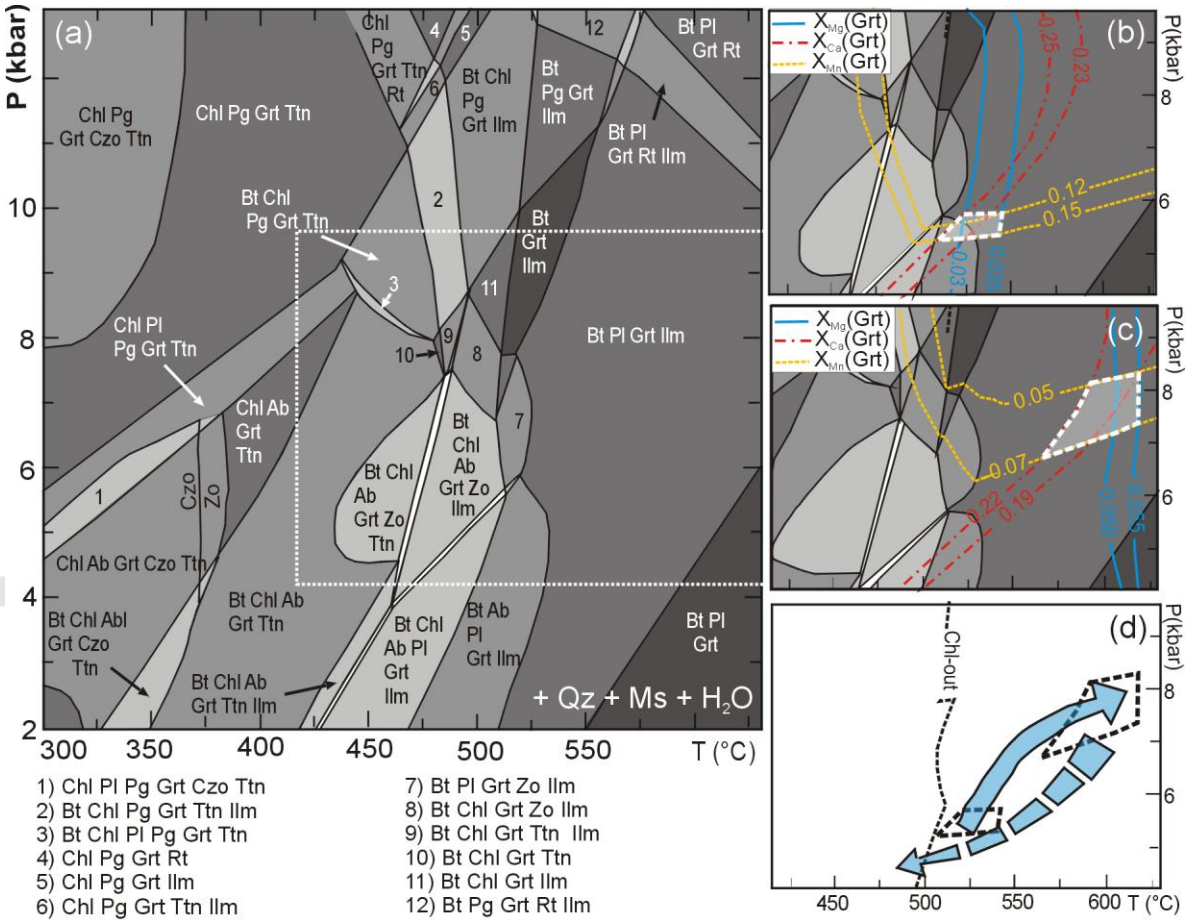

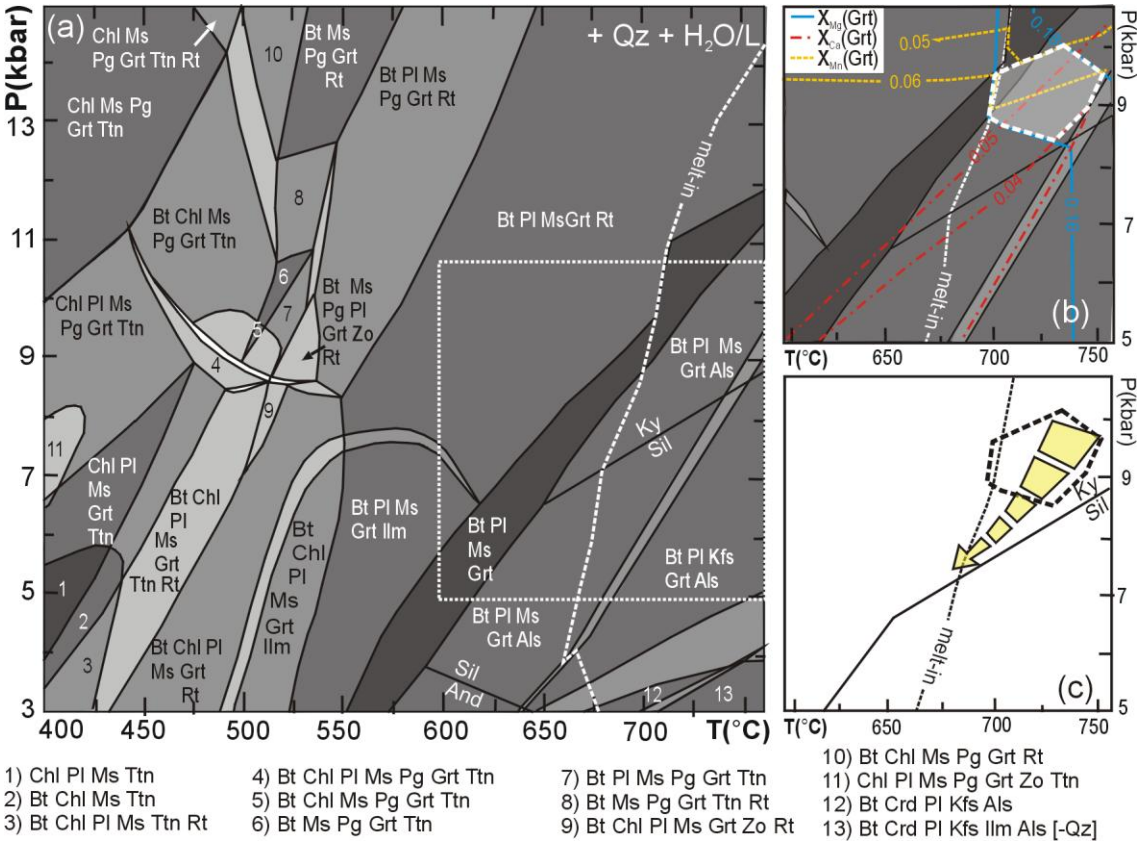

1) Chl Pl Ms Ttn
2) Bt Chl Ms Ttn
3) Bt Chl Pl Ms Ttn Rt
4) Bt Chl Pl Ms Pg Grt Ttn
5) Bt Chl Ms Pg Grt Ttn
6) Bt Ms Pg Grt Ttn
7) Bt Pl Ms Pg Grt Ttn
8) Bt Ms Pg Grt Ttn Rt
9) Bt Chl Pl Ms Grt Zo Rt
10) Bt Chl Ms Pg Grt Rt
11) Chl Pl Ms Pg Grt Zo Ttn
12) Bt Crd Pl Kfs Als
13) Bt Crd Pl Kfs Ilm Als [-Qz]